

Journal of the Atmospheric Sciences
Sounding-Based Thermodynamic Budgets for DYNAMO
 --Manuscript Draft--

Manuscript Number:	
Full Title:	Sounding-Based Thermodynamic Budgets for DYNAMO
Article Type:	Article
Corresponding Author:	Richard H. Johnson, Ph.D. Colorado State University Fort Collins, CO UNITED STATES
Corresponding Author's Institution:	Colorado State University
First Author:	Richard H. Johnson, Ph.D.
Order of Authors:	Richard H. Johnson, Ph.D. Paul E. Ciesielski James H. Ruppert, Jr. Masaki Katsumata
Abstract:	The DYNAMO (Dynamics of the MJO) field campaign, conducted over the Indian Ocean from October 2011 to March 2012, was designed to study the initiation of the Madden-Julian Oscillation (MJO). Two prominent MJOs occurred in the experimental domain during the Special Observing Period in October and November. Data from a northern and a southern sounding array (NSA and SSA, respectively) have been used to investigate the apparent heat sources and sinks (Q_1 and Q_2) and radiative heating rates Q_R throughout the life cycles of the two MJO events. The MJO signal was far stronger in the NSA than the SSA. Time series of Q_1 , Q_2 , and the vertical eddy flux of moist static energy reveal an evolution of cloud systems for both MJOs consistent with prior studies: shallow, non-precipitating cumulus during the suppressed phase, followed by cumulus congestus, then deep convection during the active phase, and finally stratiform precipitation. However, the duration of these phases was shorter for the November MJO than for the October event. The profiles of Q_1 and Q_2 for the two arrays indicate a greater stratiform rain fraction for the NSA than the SSA, a finding supported by TRMM measurements. Surface rainfall rates and Q_R determined as residuals from the budgets show good agreement with satellite-based estimates. The column-integrated Q_R anomaly was nearly 20% of the net-tropospheric convective heating anomaly for the October MJO, approaching the proposed condition for radiative-convective instability. The ratio was far less for the November event, further emphasizing important distinctions between the two MJOs.
Suggested Reviewers:	

Cost Estimation and Agreement Worksheet

[Click here to download Cost Estimation and Agreement Worksheet: Cost Estimation and Agreement Worksheet.pdf](#)

ABSTRACT

4
5 The DYNAMO (Dynamics of the MJO) field campaign, conducted over the Indian Ocean
6 from October 2011 to March 2012, was designed to study the initiation of the Madden-Julian
7 Oscillation (MJO). Two prominent MJOs occurred in the experimental domain during the
8 Special Observing Period in October and November. Data from a northern and a southern
9 sounding array (NSA and SSA, respectively) have been used to investigate the apparent heat
10 sources and sinks (Q_1 and Q_2) and radiative heating rates Q_R throughout the life cycles of the
11 two MJO events. The MJO signal was far stronger in the NSA than the SSA. Time series
12 of Q_1 , Q_2 , and the vertical eddy flux of moist static energy reveal an evolution of cloud
13 systems for both MJOs consistent with prior studies: shallow, non-precipitating cumulus
14 during the suppressed phase, followed by cumulus congestus, then deep convection during
15 the active phase, and finally stratiform precipitation. However, the duration of these phases
16 was shorter for the November MJO than for the October event. The profiles of Q_1 and Q_2
17 for the two arrays indicate a greater stratiform rain fraction for the NSA than the SSA,
18 a finding supported by TRMM measurements. Surface rainfall rates and Q_R determined
19 as residuals from the budgets show good agreement with satellite-based estimates. The
20 column-integrated Q_R anomaly was nearly 20% of the net-tropospheric convective heating
21 anomaly for the October MJO, approaching the proposed condition for radiative-convective
22 instability. The ratio was far less for the November event, further emphasizing important
23 distinctions between the two MJOs.

1. Introduction

The Madden-Julian Oscillation (MJO; Madden and Julian 1972) is one of the most prominent features of the general circulation, having global impacts on weather and climate (Zhang 2013). Despite the considerable attention given to the MJO in recent years, there remain significant gaps in understanding and prediction of the phenomenon (Hung et al. 2013; Zhang et al. 2013). A field campaign was conducted over the Indian Ocean from October 2011 to March 2012 to investigate a number of the outstanding issues related to the MJO, with particular attention to tropospheric moistening processes, evolving cloud populations, and air-sea interaction during its initiation. The experiment consisted of four collaborating campaign components (Yoneyama et al. 2013): DYNAMO (Dynamics of the MJO); CINDY (Cooperative Indian Ocean experiment on intraseasonal variability in the Year 2011); AMIE (ARM MJO Investigation Experiment); and LASP (Littoral Air-Sea Processes). Hereafter, we will refer to the combined effort as DYNAMO.

Emerging from MJO studies over the past several decades is the concept of a distinct, repeatable evolution of precipitation systems within the MJO convective envelope. Namely, cloud populations through the MJO life cycle have been observed where the dominant mode of convection transitions from shallow cumulus to cumulus congestus to deep convection to stratiform precipitation systems (Johnson et al. 1999; Kikuchi and Takayabu 2004; Benedict and Randall 2007; Haertel et al. 2008; Del Genio et al. 2012). This pattern of evolution is found to occur over a wide range of time and space scales and associated with a variety of tropical disturbances, ranging from individual convective systems to the MJO itself (Kiladis et al. 2005, 2009). Within the framework of the MJO, the pattern is characterized by changing frequency distributions of cloud types through the overall life cycle rather than one cloud type existing in each MJO phase, supportive of the “building block” hypothesis proposed by Mapes et al. (2006). Moreover, there is evidence from the studies of Kikuchi and Takayabu (2004), Yoneyama et al. (2008), Virts and Wallace (2010), Del Genio et al. (2012), and Johnson and Ciesielski (2013) to indicate that the progression of the cloud population

51 in the build-up phase of the MJO actually occurs in a stepwise fashion, with distinct periods
52 of \sim week or more when there is a dominance of each (cumulus, congestus, cumulonimbus)
53 cloud type.

54 DYNAMO was designed to explore moistening processes and cloud populations within
55 the MJO using multiple instrument platforms: cloud and precipitation radars, profilers,
56 sounding networks, aircraft, and satellites. This study focuses primarily on one aspect of the
57 DYNAMO measurement system – the sounding network – to compute heat and moisture
58 budgets following the procedures of Yanai et al. (1973), with the goal of inferring properties
59 of convective systems and their roles of latent heating and moistening/drying within the
60 MJO. While there have been numerous studies investigating diabatic heating in the MJO
61 using reanalysis data (for a review, see Zhang et al. 2013), model-independent computations
62 of MJO heating profiles from field campaigns are limited.

63 The first opportunity to directly compute heating profiles and moistening processes within
64 the MJO using a network of soundings was for the 1992-93 TOGA COARE (Tropical Ocean
65 Global Atmosphere Coupled Atmosphere-Ocean Response Experiment; Webster and Lukas
66 1992). These studies revealed a population of cloud systems within the MJO, progressing
67 from shallow cumulus, to congestus, to deep convection to stratiform through the life cycle
68 (Lin and Johnson 1996; Johnson and Lin 1987; Johnson et al. 1999; Tung et al. 1999).
69 Diabatic heating profiles were also determined for the 2006 MISMO (Mirai Indian Ocean
70 cruise for the Study of the Madden-Julian oscillation (MJO)-convection Onset; Yoneyama
71 et al. 2008). Katsumata et al. (2011) found profiles of apparent heat source Q_1 and apparent
72 moisture sink Q_2 during MISMO for an abortive MJO similar to those for TOGA COARE.

73 DYNAMO affords a third opportunity to investigate heating and moistening within the
74 MJO, but this time with improved sounding instrumentation compared to TOGA COARE
75 (Ciesielski et al. 2014a) and with higher time-resolution launches (most sites in the core
76 DYNAMO domain had three-hourly soundings as opposed to six-hourly in TOGA COARE).
77 In this study, we compute the apparent heat source Q_1 and apparent moisture sink Q_2

78 of Yanai et al. (1973) for the DYNAMO sounding arrays and combine the results with
79 independent estimates of surface fluxes to compute surface precipitation and net-tropospheric
80 radiative heating rates for the months of October and November 2011. Two prominent
81 MJO events occurred during this period (Gottschalck et al. 2013; Yoneyama et al. 2013;
82 Johnson and Ciesielski 2013). The findings are then compared to satellite-based estimates
83 of those quantities. The DYNAMO sounding array analyses have already formed the basis
84 for large-scale forcing fields being used by various authors, so evaluation of the accuracy of
85 those analyses through comparison with independent estimates is important. The analysis
86 products developed in this study have been recently used by Sobel et al. (2014) to investigate
87 the moist static energy budget for the DYNAMO MJOs.

88 Observations collected on Gan Island during AMIE have enabled the computation of the
89 vertical profile of radiative heating in the troposphere at that location as a function of time
90 throughout the experiment (Feng et al. 2014). We use these estimates of the radiative heating
91 profile to determine time series of the vertical flux of moist static energy, which provides a
92 measure of cumulus activity (Yanai et al. 1973). This information, along with the fields of
93 Q_1 and Q_2 , will be used to infer characteristics of the evolving cloud populations during
94 the DYNAMO MJOs. In addition, the possible role of radiative-convective instability in the
95 MJO (Yu et al. 1998; Raymond 2001; Stephens et al. 2004; Lin and Mapes 2004; Jiang et al.
96 2011) will be explored based on comparison of column-integrated radiative and convective
97 heating rates for the two MJOs. Further work is underway to relate the budget results to
98 cloud populations as determined by the research radars, but that effort is awaiting additional
99 quality control and evaluation of the radar products.

2. Data and analysis procedures

a. Sounding observations

The DYNAMO sounding network was composed of two quadrilateral arrays, one north and one south of the equator, referred to as the Northern and Southern Sounding Arrays or NSA and SSA, respectively (Fig. 1). Details of the sounding systems, observing characteristics, and quality-control procedures are contained in Ciesielski et al. (2014a). Incorporated into our analyses are corrections for flow distortion and island heating effects by the mountainous island of Sri Lanka on Colombo soundings (Ciesielski et al. 2014b). Blockage of the low-level flow by the island terrain frequently disrupts the winds at Colombo below about 2 km. This local effect is aliased onto larger scales and impairs computations of divergence over the NSA. The procedure developed by Ciesielski et al. (2014b) mitigates the impacts of Sri Lanka flow blocking on budgets over the NSA by using ECMWF Operational Analysis (OA) data away from the island to estimate what the wind, temperature, and moisture would be in the lowest 2 km at Colombo were the island not present.

The previous study of the thermodynamic and kinematic fields during the DYNAMO Special Observing Period or SOP (October and November 2011) by Johnson and Ciesielski (2013) was based on a preliminary version of the sounding data, which did not include corrections for humidity sensor biases at all sites. This study uses the complete set of corrections for humidity biases based on a procedure described in Ciesielski et al. (2014a). In DYNAMO, Vaisala RS92 systems were used at five of the six SSA and NSA sites, while Colombo used a Meisei system. The humidity biases for the RS92s have been found to be relatively small, namely, daytime dry biases of $\sim 2\%$ in the lower troposphere and 5-6% in the upper troposphere, which are only a third of the magnitude of the biases for the Vaisala RS80 sensors used in TOGA COARE (Wang et al. 2002; Ciesielski et al. 2003).

In addition to upsonde data, dropsonde data from the National Oceanic and Atmospheric Administration (NOAA) P-3 aircraft were incorporated into the gridded analyses described

126 below. There were 469 dropsonde observations from thirteen flights in proximity to the
127 sounding arrays during the period 9 November-13 December.

128 To supplement conventional sounding winds, two sources of satellite winds were em-
129 ployed. First, surface winds over the ocean were obtained from the Advanced Scatterometer
130 (ASCAT) on the MetOP-A satellite, which provides wind estimates nominally twice per day
131 (3-6 UTC and 15-18 UTC over the Indian Ocean) on a 12.5-km grid (Figa-Saldaña et al.
132 2002). To facilitate their use in our objective analysis, non-rain contaminated Level 2 AS-
133 CAT winds were averaged into 3-h, 2.5° bins. In addition to these surface winds, we utilized
134 upper-level atmospheric motion vector data derived from Meteosat-7 visible, infrared and
135 water vapor data (Holmlund et al. 2001) produced by the Cooperative Institute of Meteo-
136 rological Studies (CIMSS). For our analysis, these hourly wind vectors were averaged into
137 3-h, 25-hPa, 5° -resolution bins and used, only if at least three high-quality wind observations
138 were present in a given bin. With this criterion, averaged satellite winds over the central
139 Indian Ocean were available at 5° resolution $>80\%$ of the time for levels between 300 and
140 175 hPa and $\sim 20\%$ of the time for levels between 825 and 775 hPa with few observations at
141 other levels.

142 Sounding thermodynamic data were supplemented with radio occultation (RO) profiles
143 of T and T_d from the COSMIC wetPrf product based on a 1-D variational analysis using
144 ECMWF analysis as a first guess (Kuo et al. 2004). There were approximately ten COSMIC
145 profiles per month over each $5^\circ \times 5^\circ$ box over the Indian Ocean. Because of the well-
146 documented negative refractivity bias in the tropical lower-troposphere of RO soundings
147 (Ao et al. 2003), no T_d information from this product was used below 850 hPa.

148 *b. Other data sources*

149 Precipitation rates derived from the sounding budgets are compared to estimates from
150 several different sources. One is the TRMM (Tropical Rainfall Measuring Mission) 3B42v7
151 product, which combines microwave rainfall estimates from TRMM and other satellites with

152 high temporal resolution infrared rain rate estimates to create a 3-hourly, $0.25^\circ \times 0.25^\circ$ rain-
153 fall data set (Huffman et al. 2007). Other sources are the NOAA CPC Morphing Technique
154 or CMORPH (Joyce et al. 2004), available on a 0.07° grid and at 30-min time resolution; the
155 Global Precipitation Climatology Project (GPCP) with daily values on a 0.25° grid (Adler
156 et al. 2003); and the Global Satellite Mapping of Precipitation (GSMaP) with hourly values
157 on a 0.10° grid (Kubota et al. 2007; Aonashi et al. 2009).

158 Fractional cloudiness and radiation data are obtained from the Clouds and the Earth's
159 Radiant Energy System (CERES) product at 3-hourly intervals on a 1° grid (Wielicki et al.
160 1996) and the Pacific Northwest National Laboratory (PNNL) Combined Retrieval (Com-
161 bRet) product based on cloud and thermodynamic profile measurements at Gan Island (Feng
162 et al. 2014). The CombRet product is only available from 10 October onward.

163 ECMWF OA at 0.25° horizontal resolution, 18 vertical levels from the surface to 50 hPa,
164 and six-hourly intervals are used to help constrain and extend the sounding-based analyses
165 beyond the NSA and SSA domains. Unlike TOGA COARE, soundings outside the core
166 DYNAMO area were extremely sparse, so such a procedure is needed to supplement the
167 soundings. Furthermore, the ECMWF analyses were utilized to replace sounding data from
168 ships when they were off station since the quality of the analyses is degraded when the
169 network collapses from a quadrilateral to a triangle (Katsumata et al. 2011). Procedures
170 for incorporating ECMWF OA in a way that enhances the analysis but minimally impacts
171 derived fields such as divergence are described in the next subsection.

172 Surface fluxes and SST fields over the Indian Ocean are from the TropFlux product (daily
173 values, 1° horizontal grid) based on Kumar et al. (2012). To check the reliability of the
174 TropFlux data for DYNAMO, surface fluxes and SST from that product are compared to in
175 situ measurements from the R/V *Revelle*, made available via <ftp://dynamo.dms.uconn.edu/>
176 through a collaborative effort between NOAA/Physical Sciences Division/ESRL, Oregon
177 State University, and the University of Connecticut.

179 While the sounding sites comprising the SSA conducted 8-per-day launches (Fig. 1), the
180 two northern sites – Malé and Colombo – had a nominal launch frequency of 4 per day.
181 Since there is a considerable interest in the diurnal cycle over both arrays (to be reported on
182 in a companion paper, Ruppert and Johnson (2014), submitted to the *J. Atmos. Sci.*), the
183 6-hourly Malé and Colombo sounding data have been linearly interpolated in time to allow
184 for budgets to be carried out at 3-hourly intervals over both the NSA and SSA. Interpolated
185 soundings were only created if the time gap between soundings was less than or equal to the
186 nominal 6-hourly sounding interval. The interpolation procedure was also used to fill in a
187 handful of 6-h gaps in sounding data for the SSA. An evaluation of the impact of this proce-
188 dure at Gan Island where 3-hourly soundings were taken throughout the experiment shows
189 that the interpolation procedure results in relatively small errors. Specifically, rms differ-
190 ences in temperature, specific humidity, and winds between contemporaneous interpolated
191 and actual soundings are ~ 0.5 C, 0.5 g kg⁻¹, and 1 m s⁻¹, respectively.

192 Owing to the large data-void regions outside the core sounding arrays, the ECMWF OA
193 was used at 5° grid intersections if no observations (soundings, satellite winds or otherwise)
194 were present within a 4.5° radius of such an intersection. To facilitate its use at 3-h inter-
195 vals, the ECMWF OA was linearly interpolated in time to create a 3-h resolution product.
196 *Since this procedure to enhance data coverage was only applied outside the main core arrays,*
197 *results in the interior are largely independent of model analyses and hence parameterizations*
198 *of physical processes*, as will quantitatively demonstrated in Section 6a. One exception is
199 when ships were offsite, in which case model analyses filled in for missing ship soundings.
200 Only during these periods did the model analyses noticeably impact budget quantities over
201 the arrays. In recognition of the fact that the results have model influence during these
202 periods, port-call intervals are specifically denoted in time series plots by shading or other
203 designations.

204 Following interpolation to 3-hourly intervals, the sounding data, along with the other

205 observations and model fields described above, were objectively analyzed onto a 1° by 1°
 206 grid at 25-hPa intervals from 1000 to 50 hPa over the entire domain shown in Fig. 1 using
 207 the multiquadric interpolation procedure as described in Ciesielski et al. (1997). Quality-
 208 controlled sounding data from sites shown in Fig. 1 outside the arrays were used to help
 209 constrain the analyses. Corrections to the divergence were made such that vertical motion
 210 balanced to zero at the tropopause level (typically at 100 hPa), which was determined at
 211 each grid point and time step (Johnson and Ciesielski 2002).

212 3. Budget analysis considerations

213 Following Yanai et al. (1973), but including ice processes, we write the equations for the
 214 apparent heat source and moisture sink as follows:

$$\begin{aligned}
 Q_1 &\equiv \frac{\partial \bar{s}}{\partial t} + \bar{\mathbf{v}} \cdot \nabla \bar{s} + \bar{\omega} \frac{\partial \bar{s}}{\partial p} \\
 &= L_v(\bar{c} - \bar{e}) + (L_v + L_f)(\bar{d} - \bar{s}_*) + L_f(\bar{f} - \bar{m}) + Q_R - \frac{\partial}{\partial p}(\overline{s'\omega'}), \quad (1)
 \end{aligned}$$

$$\begin{aligned}
 Q_2 &\equiv -L_v \left[\frac{\partial \bar{q}}{\partial t} + \bar{\mathbf{v}} \cdot \nabla \bar{q} + \bar{\omega} \frac{\partial \bar{q}}{\partial p} \right] \\
 &= L_v(\bar{c} - \bar{e}) + L_v(\bar{d} - \bar{s}_*) + L_v \frac{\partial}{\partial p}(\overline{q'\omega'}), \quad (2)
 \end{aligned}$$

215 where c , e , d , s_* , f , and m are condensation, evaporation, deposition, sublimation, freezing,
 216 and melting rates; q is the water vapor mixing ratio; $s \equiv c_p T + gz$ the dry static energy; Q_1
 217 the apparent heat source; Q_2 the apparent moisture sink; Q_R the net radiative heating rate;
 218 L_v and L_f the latent heats of vaporization and fusion; overbar refers to a horizontal average;
 219 primes a deviation from this average; and horizontal eddy flux divergences are assumed to
 220 be small.¹

¹A more accurate representation of the moist thermodynamics includes conservation equations for vapor

221 Integration of (1) and (2) from the tropopause pressure p_T to surface pressure p_0 yields

$$\langle Q_1 \rangle = \langle Q_R \rangle + L_v P_0 + \langle L_f(\bar{d} - \bar{s}_*) \rangle + \langle L_f(\bar{f} - \bar{m}) \rangle + S_0 \quad (3)$$

$$\langle Q_2 \rangle = L_v(P_0 - E_0) , \quad (4)$$

222 where $\langle \quad \rangle \equiv 1/g \int_{p_T}^{p_0} (\quad) dp$, the surface precipitation rate is $P_0 = \langle \bar{c} - \bar{e} + \bar{d} - \bar{s}_* \rangle$, S_0 is
 223 the surface sensible heat flux, and E_0 the surface evaporation rate. In the following analysis,
 224 it is assumed that over the large sounding arrays and long time scales considered the terms
 225 $\langle L_f(\bar{d} - \bar{s}_*) \rangle$ and $\langle L_f(\bar{f} - \bar{m}) \rangle$ in (3), for which there are no direct measurements,
 226 are comparatively small. Therefore, we make the following approximation, as in Yanai and
 227 Johnson (1993):

$$\langle Q_1 \rangle \cong \langle Q_R \rangle + L_v P_0 + S_0 . \quad (5)$$

228 As a check on this assumption, the Goddard Cumulus Ensemble modeling results of Tao
 229 et al. (2003) applied to the convectively active periods of the South China Sea Monsoon
 230 Experiment (SCSMEX) give a ratio of $\langle L_f(\bar{d} - \bar{s}_*) \rangle$ to $L_v P_0$ in (3) of ~ 0.03 , while the
 231 ratio of $\langle L_f(\bar{f} - \bar{m}) \rangle$ to $L_v P_0$ is far smaller.

232 Locally, however, e.g., averaged separately over the convective and stratiform regions of
 233 a tropical squall line, the above omitted terms are not negligible. These terms could also be
 234 important when there is a substantial build-up or decay in precipitation systems, even over
 235 large areas. For example, as convection builds up within the NSA during the developing
 236 phase of the MJO, there could be considerably more deposition than sublimation, as well
 237 as more freezing than melting, during a time interval of days, with the opposite being true
 238 during a decay phase. The latter situation is related to hydrometeor storage, which can
 and airborne condensate, precipitation mass, and the entropy of moist air (e.g., Ooyama 1990). However,
 owing to the lack of direct measurements of microphysical processes and precipitation rates over the sounding
 arrays, we use the formulation of Yanai et al. (1973).

239 be important on diurnal time scales (McNab and Betts 1978) or when the cloud volume is
 240 changing rapidly and/or when there is an advection of hydrometeors into or out of a region.
 241 An attempt was made by Johnson (1980) to estimate hydrometeor storage effects for a
 242 composite easterly wave during the GARP Atlantic Tropical Experiment, but determination
 243 of the evolving cloud and precipitation fields posed serious challenges and the computations
 244 contained considerable uncertainty. While we have future plans to utilize satellite, radar,
 245 and other data to investigate such storage effects, they are excluded from this study.

246 Defining moist static energy as $h \equiv s + L_v q$, subtraction of (2) from (1) and integration
 247 from the tropopause to any level p (neglecting the terms involving L_f) yields an expression
 248 for F , the vertical eddy flux of h :

$$F(p) \equiv -\frac{1}{g} \overline{(h'\omega')}_p \cong \frac{1}{g} \int_{p_T}^p (Q_1 - Q_2 - Q_R) dp, \quad (6)$$

249 or upon integration to the surface, we have following Yanai et al. (1973):

$$F_0 \equiv F(p_0) = S_0 + L_v E_0 \cong \langle Q_1 \rangle - \langle Q_2 \rangle - \langle Q_R \rangle. \quad (7)$$

250 An alternate version of (7) can be written as

$$\langle \frac{\partial \bar{h}}{\partial t} \rangle + \langle \bar{\mathbf{v}} \cdot \nabla \bar{h} \rangle + \langle \bar{\omega} \frac{\partial \bar{h}}{\partial p} \rangle = \langle Q_1 \rangle - \langle Q_2 \rangle \cong S_0 + L_v E_0 + \langle Q_R \rangle. \quad (8)$$

251 Sobel et al. (2014) used (8) along with the sounding data employed in this study and also
 252 ERA Interim reanalysis data to investigate the moist static energy budget for the October
 253 and November MJOs. That analysis will not be repeated here, but we will relate our findings
 254 to theirs where appropriate.

255 The above set of equations can be used to check the accuracy of the budgets. The surface
 256 precipitation rate P_0 can be estimated from the moisture or heat equations, (4) or (5), but
 257 since $\langle Q_R \rangle$ is not directly measured, and (5) is an approximation, we use (4), with E_0

258 from TropFlux, to compute P_0 and compare those values with independent satellite-based
259 estimates for the sounding arrays.

260 We use (7) to compute $\langle Q_R \rangle$, again using surface fluxes from TropFlux, and compare
261 these values with independent estimates from CERES (for the arrays) and PNNL (for Gan
262 Island). Following the procedures in Johnson and Ciesielski (2000), we also include sev-
263 eral additional effects, which act in the direction to increase, albeit slightly, the diagnosed
264 radiative cooling rate. They are (1) the effects of mass sources and sinks resulting from pre-
265 cipitation and surface evaporation on the computation of vertical motion (Trenberth 1991);
266 (2) the sensible heat flux due to rain, which falls at the wet-bulb temperature (Gosnell et al.
267 1995); and (3) frictional dissipation associated with falling precipitation (Emanuel and Bister
268 1996).

269 In past budget studies, we did not have sufficient information on the vertical structure
270 of Q_R to compute the vertical profile of F . For DYNAMO, however, we have the PNNL
271 CombRet product that provides the vertical profile of Q_R (Feng et al. 2014), so $F(p)$ can
272 be computed. Unfortunately, cloud measurements taken at the AMIE site on Gan Island
273 undersampled high-level cirrus clouds due to signal attenuation in heavy rainfall, so their
274 effects are not fully represented in the CombRet radiative heating rates. As a result, the
275 CombRet net-tropospheric radiative cooling during the cirrus-abundant convectively active
276 phase of the MJO is somewhat overestimated compared to the CERES product, as will be
277 shown later. Therefore, for the computation of F , we adjust the profile of Q_R from CombRet
278 by a constant fraction at each level so that its vertical integral matches that of the CERES
279 product. Ideally, this adjustment should be distributed vertically in a realistic way, but we
280 do not have sufficient information to do so at this time.

281 4. Broad-scale distributions of rainfall

282 a. Surface flux estimates used in rainfall computations

283 Computations of precipitation and radiative heating rates over the arrays rely on es-
284 timates of surface fluxes over the enclosed areas. Two flux products have been tested:
285 the Woods Hole Oceanographic Institution (WHOI) Objectively Analyzed air-sea Fluxes
286 (OAFlux) based on Yu and Weller (2007) and TropFlux (Kumar et al. 2012). Similar results
287 were obtained for both products; however, since TropFlux yields slightly better correlations
288 of computed rainfall rates to those observed, we employ that product for the following anal-
289 yses.

290 To evaluate the accuracy of TropFlux for DYNAMO, surface fluxes from that product
291 are compared to bulk fluxes at the R/V *Revelle* computed using the COARE 3.0 algorithm
292 (Fairall et al. 1996). The mean of TropFlux values that fall within a 1° radius of *Revelle's*
293 nominal position are plotted in Fig. 2 along with daily-averaged *Revelle* fluxes when the ship
294 is on station. SST from the *Revelle* are also shown in Fig. 2, as is the mean TRMM rainfall
295 within the 1° radius of the site. The surface sensible and latent heat fluxes and SST, both
296 the daily and SOP-mean values, all show good agreement throughout the period. SOP-mean
297 values of S_0 , $L_v E_0$, and SST are $10\text{-}11 \text{ W m}^{-2}$, $106\text{-}107 \text{ W m}^{-2}$, and 29.5°C , respectively.
298 These values are in close agreement with the those reported over the western Pacific during
299 TOGA COARE (Weller and Anderson 1996).

300 b. Large-scale temporal and spatial distributions of rainfall

301 Using surface latent heat fluxes over the Indian Ocean from TropFlux, 3-day running
302 mean filtered daily-average rainfall rates computed from (4) are compared to TRMM 3B42
303 estimates (3-hourly, unfiltered) in Fig. 3. In the longitude band of the sounding arrays
304 ($72\text{-}80^\circ\text{E}$), the analysis is based on the sounding data whereas outside the arrays, it is based
305 principally on the ECMWF OA. Though peak amplitudes in the moisture budget are reduced

306 by the filtering, the spatial and temporal distribution of budget estimates agree well with
307 the TRMM envelopes of convection for the two MJO events in October and November. This
308 filtered version of the budget analysis does not capture the higher-frequency disturbances
309 embedded within the MJOs (Gottschalck et al. 2013), such as the two-day disturbances
310 within the active phase of the MJO in October (Zuluaga and Houze 2013; Johnson and
311 Ciesielski 2013). Analyses of the heat and moisture budgets for these disturbances is left for
312 future work.

313 A broad-scale depiction of the SOP-mean rainfall rate over the Indian Ocean for October
314 and November is presented in Fig. 4. Rainfall rate diagnosed from the moisture budget is
315 in overall good agreement with the TRMM estimates both in terms of magnitude and areal
316 distribution. A prominent feature of the rainfall pattern is an ITCZ-like band between the
317 equator and 10°S extending across much of the Indian Ocean. Slightly greater SOP-mean
318 rainfall rates can be seen over the SSA than the NSA in both TRMM (9.0 vs. 8.7 mm day⁻¹)
319 and the budgets (10.4 vs. 9.2 mm day⁻¹).

320 **5. Heat and moisture budgets for sounding arrays**

321 *a. Time series for Special Observing Period (SOP)*

322 Time series of the apparent heat source Q_1 and apparent moisture sink Q_2 over the NSA
323 for October and November are shown in Fig. 5, along with NSA daily-mean rainfall from
324 TRMM. The MJO heavy-rain periods in the latter half of both months are accompanied by
325 pronounced increases in the amplitudes of Q_1 and Q_2 . The timing of the peaks in both fields
326 correspond well to peaks in rainfall, lending confidence to the budget results for the NSA
327 (more detailed comparisons will be given later). It should be noted that as expected, the
328 rainfall time series for the entire NSA (Fig. 5) does not correlate well with that for a single
329 location, namely, at the *Revelle* (Fig. 2), but it does represent well the convectively active
330 periods of the October and November MJOs (Fig. 3).

331 The evolution of Q_1 and Q_2 through both MJO events shows a similar progression to
332 that observed during TOGA COARE (Lin and Johnson 1996): shallow, non-precipitating cu-
333 mulus indicating lower-tropospheric moistening (negative Q_2) during the non-rainy periods,
334 followed by cumulus congestus (low-to-midlevel peaks in Q_1 and Q_2), then deep convection
335 (higher peaks in Q_1 and Q_2), and finally stratiform-like profiles of Q_1 and Q_2 (positive val-
336 ues aloft, negative at low levels). This progression is consistent with now generally accepted
337 paradigm for the evolution of precipitation systems and diabatic heating through the life
338 cycle of the MJO (Johnson et al. 1999; Kiladis et al. 2005; Zhang 2005; Mapes et al. 2006;
339 Benedict and Randall 2007; Haertel et al. 2008). There is also evidence in the heating and
340 drying profiles (further supported by the moist static energy fluxes shown later) of a step-
341 wise progression of the cloud fields from shallow cumulus to congestus to deep convection,
342 which is evident in observations from past studies (Kikuchi and Takayabu 2004; Yoneyama
343 et al. 2008; Virts and Wallace 2010; Del Genio et al. 2012) and also recognizable in the time
344 series of relative humidity at Malé, Gan Island, and the R/V *Revelle* (Fig. 13 of Johnson
345 and Ciesielski 2013). A notable difference between the two events, however, is the longer
346 duration of both the build-up and convectively active periods for the October case compared
347 to the November MJO. In addition, the convective moistening by shallow cumulus during
348 the suppressed periods was stronger for the October than the November event.

349 The time series of Q_1 and Q_2 over the SSA (Fig. 6) contrasts markedly to that over the
350 NSA even though both arrays share the common sites Gan Island and *Revelle*. As noted
351 in Johnson and Ciesielski (2013), the MJO signal during the October-November period of
352 DYNAMO was stronger north of the equator during this boreal fall period. Frequent episodes
353 of rainfall corresponding to periods of heating/drying occurred throughout the two-month
354 period with a moderate increase in convective activity associated with the MJOs toward the
355 ends of October and November. As can be seen from Fig. 4, the SSA straddled an ITCZ-like
356 band of precipitation between the equator and 10°S , which is reflected in the semi-permanent
357 precipitation in that array.

358 *b. Mean profiles for SOP*

359 SOP-mean vertical profiles of Q_1 and Q_2 for the NSA and SSA, along with frequency-
360 altitude diagrams for each, are shown in Fig. 7. The amplitudes of the profiles are similar be-
361 tween the two arrays, consistent with the approximate agreement in TRMM 3B42-estimated
362 rainfall for the NSA (8.7 mm day^{-1}) and SSA (9.0 mm day^{-1}). The Q_1 and Q_2 profile
363 shapes are similar over the NSA, while the peaks are widely separated over the SSA. These
364 results suggest a greater fraction of stratiform precipitation over the NSA than the SSA (e.g.,
365 Luo and Yanai 1984). This inference is supported by the frequency-altitude diagrams for the
366 NSA (Fig. 7), which show a greater spread of negative Q_2 values (indicative of moistening by
367 evaporation) and a higher frequency of negative Q_1 values (cooling) in the lower troposphere
368 than for the SSA. Three research radars were deployed in DYNAMO, but their precipitation
369 area coverage is very small compared to the areas of the sounding arrays, so they cannot
370 be used to check the inference of greater stratiform rain fraction over the NSA. Analysis
371 of the convective/stratiform fractions from the TRMM 2A25 product does show a greater
372 stratiform fraction for the NSA (55%) than the SSA (50%), although the sampling for the
373 two-month period is limited. In particular, there were 102 (117) TRMM overpasses for the
374 NSA (SSA) during the SOP. These TRMM stratiform fractions are greater than the tropical
375 global estimate of $\sim 40\%$ (Schumacher and Houze 2003).² However, the TRMM estimates
376 for DYNAMO do show a greater stratiform contribution to rainfall over the NSA than the
377 SSA, which is consistent with the budget findings. Considering that the MJO signal was
378 stronger over the NSA than the SSA (Johnson and Ciesielski 2013), these findings are also
379 consistent with the results of Lin et al. (2004) that indicate a greater stratiform rain fraction
380 within the MJO convective envelope than the tropical mean.

²This estimate was recently revised downward to $\sim 35\%$ by Funk et al. (2013) based on a consideration of misclassification of some shallow clouds as stratiform in the TRMM 2A23v7 algorithm.

381 6. Precipitation rate intercomparisons

382 a. Impact of ECMWF operational analysis data on budgets

383 As noted earlier, the ECMWF OA has been used outside the sounding arrays, but also
384 in proximity to the R/V *Revelle* and *Mirai* when those ships were off station in order to
385 improve the analyses during the port-call periods. To demonstrate this improvement, and
386 also show the minor effects of the model analyses at other times, a time series of rainfall
387 rate computed from the Q_2 budget for the NSA with and without ECMWF analyses is
388 shown in Fig. 8 (upper panel). Outside the port-call period, there is mostly only a minor
389 change in the rainfall estimates by the inclusion of ECMWF OA (Fig. 8, lower panel),
390 supporting the assertion of minimal impact of model analyses when all sites were occupied.
391 A similar comparison of the divergence profiles (not shown) indicates little impact by the
392 model analyses during that period. Overall, the budget and TRMM rainfall rates agree well,
393 and the agreement during the port-call period improves with the inclusion of ECMWF OA
394 (values are generally overestimated without ECMWF OA). Averaged over the entire SOP,
395 the addition of ECMWF OA brings the NSA mean budget rainfall rate (9.2 mm day^{-1}) more
396 in line with the TRMM estimate (8.7 mm day^{-1}). The budget estimate for the NSA area
397 and for the two-month period corresponding to the SOP is subject to a random sampling
398 error of 0.3 mm day^{-1} based on the work of Mapes et al. (2003).

399 b. Intercomparison of budget and satellite estimates

400 A comparison between the budget rainfall estimates and those for four different satellite
401 products is shown in Fig. 9 and Table 1 for both the NSA and SSA. There is good agreement
402 among the various satellite products and the budgets for the NSA: satellite estimates ranging
403 from 8.7 to 9.7 mm day^{-1} compared to the budget 9.2 mm day^{-1} . The agreement is slightly
404 poorer for the SSA: 8.1 to 9.6 mm day^{-1} compared to the budget 10.4 mm day^{-1} . For the
405 NSA, temporal correlations between budget estimates and TRMM, CMORPH, GPCP, and

406 GSMP (all with 3-day running-mean filtering of daily-average values) are 0.97, 0.96, 0.92,
 407 and 0.93, respectively. The correlations for the SSA are not quite as good: 0.92, 0.90, 0.83,
 408 and 0.86, respectively, for the same products. We do not have an explanation for the poorer
 409 overall agreement for the SSA, except that the area straddles a persistent ITCZ band of
 410 convection and hence may be more impacted by nonlinear variation of the fields between
 411 sounding sites. The mean NSA budget rainfall rate for the DYNAMO SOP (9.2 mm day^{-1})
 412 is comparable to the mean value of 8.4 mm day^{-1} for the four-month Intensive Observing
 413 Period (IOP) of the TOGA COARE Intensive Flux Array (IFA) (Table 1). The correlations
 414 between the budget and satellite-based rainfall estimates for DYNAMO, all exceeding 0.90
 415 for the NSA, represent an improvement over the TOGA COARE IFA budget and satellite
 416 rainfall rate correlations that were closer to 0.80 (Ciesielski et al. 2003).

417 Also seen in Fig. 9 are the possible effects of hydrometeor storage on the budgets (McNab
 418 and Betts 1978; Johnson 1980), particularly over the NSA for the October MJO. During the
 419 period of increasing precipitation between October 15 and 22, the budget rainfall rate exceeds
 420 the all of the satellite estimates, but the reverse is true toward the end of October. The
 421 discrepancy for the 15-22 October period may be related to the storage of water in clouds
 422 as the cloud area increased rapidly (Fig. 12, later), whereas the reverse situation at the end
 423 of the month is presumably a result of evaporation of cloud systems generated at an earlier
 424 time as the cloud area decreased rapidly (Fig. 12 again). Evidence of storage effects is not
 425 as obvious for the November MJO.

426 7. Intercomparison of radiative heating rates

427 a. Budget-satellite intercomparisons, relationship to cloud cover

428 In this section we compare $\langle Q_R \rangle$ obtained from the combined heat and moisture
 429 budgets and surface fluxes (7) with the CERES and PNNL radiation products. However, we
 430 first show a time series of the vertical profile of Q_R from the PNNL CombRet product for

431 Gan Island (Feng et al. 2014), along with three-month mean values of shortwave, longwave,
 432 and net radiative heating (Fig. 10). The October and November MJOs are clearly seen to
 433 modulate Q_R , as does another MJO-like event in December described by Gottschalck et al.
 434 (2013) and Yoneyama et al. (2013). During the convectively active phases in the latter halves
 435 of the months, greatly reduced net radiative cooling, even reverting to a net heating at times,
 436 is seen to occur in the midtroposphere in response to the increased upper-level cloud cover
 437 (shown later). In the upper troposphere between 400 and 200 hPa, intermittent enhanced
 438 cooling can be seen, reflecting increased longwave cooling atop upper-level cloud systems.
 439 However, the overall cooling in this layer is likely overestimated due to the undersampling
 440 of cirrus clouds by the instrumentation on Gan Island (Feng et al. 2014). This conclusion is
 441 supported by the study of Jiang et al. (2011), which shows a similar modulation of Q_R by the
 442 MJO from the TRMM-based radiation algorithm of L’Ecuyer and McGarragh (2010), but
 443 the maximum heating (i.e., minimum cooling) during the convectively active phases is shifted
 444 upward to near 300 hPa as opposed to the peaks being centered more in the midtroposphere
 445 in the CombRet product. The mean profile of Q_R shows a ~ 1 K day $^{-1}$ net cooling averaged
 446 through the troposphere, with slightly greater cooling near the surface and in the upper
 447 troposphere.

448 SOP time series of $\langle Q_R \rangle$ from the budgets and other independent estimates for the
 449 NSA and SSA, along with SOP-mean values, are shown in Fig. 11 and Table 1. The budget
 450 and CERES results are for the array areas, while the CombRet estimate is for the Gan Island
 451 location only. Two curves are shown for the budget results, one with the inclusion of the
 452 effects of precipitation/evaporation on the computation of divergence, sensible heat flux due
 453 to rain, and frictional dissipation associated with precipitation (thick black curve) and one
 454 without (thin black curve). These effects are minor, but they bring the period-mean $\langle Q_R \rangle$
 455 values, -0.59 and -0.53 K day $^{-1}$, into closer agreement with the CERES SOP-mean values,
 456 -0.63 and -0.62 K day $^{-1}$, for the NSA and SSA, respectively (Table 1). For the array areas
 457 and two-month period of the SOP, the random sampling error for $\langle Q_R \rangle$ associated with

458 the budget results is 0.03 K day^{-1} (Mapes et al. 2003). In addition to the SOP-mean values,
459 the temporal variability of the budget and CERES $\langle Q_R \rangle$ are in generally good agreement.
460 Much-reduced net radiative cooling is observed during the active phases of both MJOs as a
461 result of the abundance of high and midlevel clouds (Fig. 12), which plays an important role
462 in increasing the column-integrated moist static energy at those times (Chikira 2014; Sobel
463 et al. 2014).

464 The budget-mean value of $\langle Q_R \rangle$ for the DYNAMO arrays is very close to the value of
465 -0.55 K day^{-1} obtained for the TOGA COARE IFA by Ciesielski et al. (2003) using the same
466 budget methodology (Table 1). In addition, the large-amplitude variation of $\langle Q_R \rangle$ over the
467 life cycles of the DYNAMO MJOs closely resembles that observed for the major December
468 1992 MJO event in TOGA COARE (Johnson and Ciesielski 2000). Past studies have shown
469 that this horizontal variability can have substantial impacts on the tropical Walker and
470 Hadley circulations (Hartmann et al. 1984; Slingo and Slingo 1988, 1991; Randall et al.
471 1989; Sherwood et al. 1994; Webster 1994; Raymond 2000). Qualitatively, the modulation
472 of $\langle Q_R \rangle$ by the MJOs is similar in the CombRet estimate, though the SOP-mean net
473 cooling rate (-0.81 K day^{-1}) is greater. This discrepancy is related to the undersampling
474 of upper-tropospheric clouds by the instrumentation on Gan Island, and hence exclusion of
475 their full effects in the radiation calculations.

476 The time series of budget and CERES $\langle Q_R \rangle$ for the NSA are repeated in Fig. 12
477 (middle panel), but to better illustrate the full cycle of the November MJO, for a slightly
478 longer period than the SOP (until December 6 when six-hourly soundings on Colombo were
479 terminated). Also included are a time series of relative humidity (upper panel) and cloud
480 fractional area from the CERES product for low, low-middle, high-middle and high clouds
481 (lower panel). Figure 12 shows a strong correlation of the net tropospheric radiative heating
482 with upper-tropospheric clouds, namely, $|\langle Q_R \rangle|$ decreases (increases) as the high clouds
483 increase (decrease). This result confirms the important role of high-level clouds in trapping
484 longwave radiation in the troposphere (e.g., Hartmann et al. 1992; Stephens et al. 1994). The

485 fractional area of shallow clouds is seen to decrease during the convectively active phases of
 486 the MJO (Zuluaga and Houze 2013); however, there may be some blocking of the satellite
 487 detection of shallow clouds by upper-level cloud layers. There is a slight increase in middle-
 488 low cloud coverage in the middle of October and November, consistent with the implied
 489 increase in congestus activity during those times from the heat and moisture budgets (Fig.
 490 5). Detailed comparisons of the budget results with cloud populations measured by the
 491 DYNAMO research radars will be reported in a later study.

492 Also evident from Fig. 12 is an increase in upper-tropospheric relative humidity in the
 493 middle of each month, consistent with the increase in high-level clouds and a corresponding
 494 reduction in $|\langle Q_R \rangle|$ that occurred at those times. As noted in Johnson and Ciesielski
 495 (2013), this moistening was associated with a cool anomaly aloft in advance of the convec-
 496 tively active phase of the MJO. The tilted warm-cool anomaly pattern that was observed
 497 during DYNAMO (Johnson and Ciesielski 2013) resembled that first described by Kiladis
 498 et al. (2001), who explained this feature as a gravity wave response to the large-scale MJO
 499 convective heat source envelope. It is consistent with the recent findings of Virts and Wallace
 500 (2010) and Virts et al. (2010), who determined from an analysis of CALIPSO cirrus data
 501 that the coldest, cloudiest anomalies aloft occur $\sim 30^\circ$ east of the main MJO convective heat
 502 source and descend with time, which is qualitatively consistent with the moisture anomalies
 503 observed during DYNAMO (Fig. 12).

504 *b. Assessment of radiative-convective instability*

505 To assess the possible role of radiative forcing in the dynamics of the MJO, a comparison is
 506 made between the anomalies of column-integrated convective heating $L_v P_0 + S_0 \equiv \langle Q_{conv} \rangle$
 507 from the budgets and flux data and $\langle Q_R \rangle$ from the CERES product for DYNAMO. The
 508 results for the NSA are shown in Fig. 13, along with a time series of precipitation for the SOP.
 509 Past work by Lin and Mapes (2004) using various budget and radiation data sets showed
 510 that for the December 1992 TOGA COARE MJO, the column-integrated radiative heating

511 lagged the column-integrated convective heating by about five days and the enhancement to
512 the convective heating was about 10-15%. This enhancement fell short of the $\sim 20\%$ Lee et al.
513 (2001) estimate as necessary for the atmosphere to reach radiative-convective instability (Yu
514 et al. 1998; Raymond 2001). Lin and Mapes (2004) speculated that the enhancement factor
515 might be larger, exceeding 20%, over the Indian Ocean and the recent study of Jiang et al.
516 (2011) using satellite and reanalysis data seems to bear this out. The enhancement factor for
517 the October MJO, 18%, does approach this threshold; however, it is considerably less, 11%,
518 for the November event. This finding highlights yet another important distinction between
519 the two DYNAMO MJOs despite broadly similar characteristics of their thermodynamic and
520 kinematic structures (Johnson and Ciesielski 2013).

521 8. Vertical flux of moist static energy

522 The vertical eddy flux of h (or F), provides a measure of the activity of cumulus con-
523 vection (Yanai et al. 1973). Given the same rainfall rate in two different settings, if F in
524 the midtroposphere is large (small), the precipitation processes producing the rainfall are
525 largely convective (stratiform). The determination of $F(p)$ as a function of time in past
526 field campaigns such as TOGA COARE has been difficult owing to the lack of knowledge
527 about vertical structure of the net radiative heating rate, $Q_R(p)$, as a function of time. As
528 noted earlier, we use the PNNL CombRet Q_R product in the computation of F , but since
529 the cooling is overestimated owing to the lack of high-cloud measurements on Gan Island,
530 we adjust the CombRet $Q_R(p)$ by a constant factor such that its vertical integral matches
531 $\langle Q_R \rangle$ from array-averaged CERES values.³ In the computation of $F(p)$, we integrate
532 downward from the tropopause assuming the eddy fluxes are zero at that level.

³CombRet data are not available for the period 1-9 October, so the vertical profiles for that period are approximated using CombRet $Q(p)$ for the period 12-17 November. Both of these periods experienced suppressed conditions and were characterized with similar budget profiles and CERES $\langle Q_R \rangle$.

533 A time series of F for the NSA is shown in Fig. 14. Several levels of deep convective
 534 activity are evident. First, in the light-rain periods during the first halves of October and
 535 November, the eddy fluxes are confined to the lower troposphere, consistent with the in-
 536 ference from Q_2 in Fig. 5 of shallow, trade-like cumulus at those times. These periods are
 537 followed by \sim five-day periods of eddy fluxes extending to the midtroposphere, indicative of
 538 cumulus congestus cloud populations (as also inferred from Fig. 5), and then later by \sim one-
 539 week periods of strong eddy fluxes extending to the upper troposphere. Consistent with the
 540 profiles of Q_1 and Q_2 in Fig. 5 the time series of relative humidity at NSA sites (Fig. 13 of
 541 Johnson and Ciesielski 2013), a stepwise evolution of the cloud populations is evident as op-
 542 posed to a smooth transition of the cloud fields. Work is currently underway to relate these
 543 results to the cloud populations as determined by the research radars. The deeper events in
 544 October were associated with westward-moving, two-day disturbances (Zuluaga and Houze
 545 2013; Johnson and Ciesielski 2013), while those in November were associated with Kelvin
 546 waves (Gottschalck et al. 2013). The light-rain periods following the active periods of heavi-
 547 est rainfall were characterized by weak eddy fluxes, consistent with a prevalence of stratiform
 548 precipitation. These results further support the accumulating evidence of a typical pattern
 549 of shallow-to-congestus-to-deep-to-stratiform evolution of precipitation within the MJO.

550 The profiles of F for the SSA are strikingly different (Fig. 15). There are numerous
 551 instances of strong eddy fluxes extending to the midtroposphere throughout the two-month
 552 period. Although there are several strong events timed with the heavy rainfall at the ends
 553 of October and November in connection with the MJOs, others occurred in the suppressed
 554 phases of the events and are related to episodic disturbances within the ITCZ-like precipi-
 555 tation band south of the equator.

556 SOP-mean profiles of Q_1 , Q_2 , Q_R , $Q_1 - Q_2 - Q_R$, and F are shown in Fig. 16 for the
 557 NSA and SSA. Once again, the substantially different mean characteristics of convection in
 558 the two arrays are evident. The smaller separation of the Q_1 and Q_2 peaks in the NSA leads
 559 to smaller values of $Q_1 - Q_2 - Q_R$ (i.e., the eddy flux convergence) in the upper troposphere

560 and weaker eddy fluxes in the midtroposphere, consistent with the higher stratiform rain
561 fraction there as supported by the TRMM estimates. Comparison of F_0 from the budgets
562 with $S_0 + L_v E_0$ from TropFlux shown in Fig 16 indicate good agreement for the NSA (128
563 vs. 115 W m^{-2} , respectively) but slightly poorer agreement for the SSA (138 vs. 116 W
564 m^{-2} , respectively).

565 9. Summary and conclusions

566 DYNAMO sounding data have been used to determine the apparent heat source Q_1
567 and apparent moisture sink Q_2 for the northern and southern sounding arrays (NSA and
568 SSA, respectively) over the central Indian Ocean during the DYNAMO Special Observing
569 Period (SOP; October–November 2011). The sounding data have undergone extensive quality
570 control prior to the computation of the budgets (Ciesielski et al. 2014a). In addition, a
571 procedure has been applied to mitigate the effects of the mountainous island of Sri Lanka on
572 the Colombo soundings (Ciesielski et al. 2014b). Although ECMWF operational analyses
573 have been used to describe the larger-scale characteristics of the flow over the Indian Ocean
574 during DYNAMO, the budget results for the sounding arrays are largely model-independent.
575 Surface precipitation rate P_0 from the moisture budget and tropospheric net radiation $<$
576 $Q_R >$ from the combined budgets have been determined by incorporating surface sensible
577 and latent heat flux measurements from TropFlux (Kumar et al. 2012). The TropFlux
578 measurements show good agreement with the in situ measurements of the bulk fluxes at the
579 R/V *Revelle*. The results for P_0 and $< Q_R >$ are compared to independent satellite-based
580 estimates of these quantities. In addition, the availability of vertical profiles of radiative
581 heating rate from the AMIE facility on Gan Island has permitted computations of the vertical
582 profile of the vertical eddy flux of moist static energy. Finally, the budget results and CERES
583 radiation data are used to assess whether radiative-convective instability was operative for
584 the MJOs during DYNAMO.

585 Principal findings of the study are as follows:

- 586 • The spatial and temporal variation of the budget-derived rainfall rate over the Indian
587 Ocean during the SOP shows good agreement with the independent TRMM-based
588 estimates. Moreover, the time series of rainfall rate from the moisture budget agrees
589 well with the satellite-based estimates (TRMM, CMORPH, GPCP, and GSMAP).

- 590 • Prominent MJO signals were observed over the NSA, with a sequence of convective sys-
591 tem evolution in a stepwise fashion inferred from Q_1 and Q_2 for both the October and
592 November MJOs consistent with numerous previous studies: shallow non-precipitating
593 cumulus, followed by congestus clouds, then deep convection, and finally stratiform
594 precipitation. The two MJOs were otherwise quite different. Stronger convective
595 moistening by shallow cumulus was observed leading up to the active phase in October
596 than November. The duration of deep convective activity was at least a week longer
597 for the October MJO, and consisted of more short duration (two-day) pulses of heat-
598 ing than in the November MJO, where two prominent Kelvin waves dominated the
599 heating.

- 600 • The time series of Q_1 and Q_2 for the SSA were strikingly different from the NSA,
601 characterized by frequent episodes of heating and drying in association with multiple
602 precipitation events. The MJO signal in the heating was still evident in the SSA, but
603 smaller in amplitude.

- 604 • The shapes of Q_1 and Q_2 vertical profiles were similar for the NSA, but less so for the
605 SSA where the peaks were widely separated, suggesting a greater stratiform rain frac-
606 tion over the NSA than the SSA. TRMM measurements support this finding, though
607 the sampling was limited. The findings support the work of Lin et al. (2004), which
608 indicates that the stratiform rain fraction for the MJO is greater than the tropical
609 mean.

- 610 • The time series of $\langle Q_R \rangle$ from the budgets agrees well with the satellite-based
611 CERES estimate, both showing a significant modulation of $\langle Q_R \rangle$ by the MJO.
612 High-level clouds during the active phases of the both MJOs reduced the net-column
613 radiative cooling, even reverting $\langle Q_R \rangle$ to weak positive values at times, indicating
614 the important role of radiation in the moist static energy budget (Sobel et al. 2014).
615 For the NSA, the budget SOP-mean $\langle Q_R \rangle$ was -0.59 K day^{-1} compared to -0.63
616 K day^{-1} for CERES, while the agreement was slightly poorer for the SSA (-0.53 vs.
617 -0.62 K day^{-1} , respectively).
- 618 • Vertical profiles of the vertical flux of moist static energy for the NSA support the
619 inferences of the evolving cloud populations in the MJO based on the Q_1 and Q_2 results
620 alone, namely, a transition from shallow cumulus to congestus to deep convection and
621 finally to stratiform precipitation. The results for the SSA are again strikingly different,
622 indicating much more frequent episodes of convective activity in the ITCZ, with an
623 absence of the convective evolution seen for the NSA.
- 624 • The ratio of the anomaly of the column-integrated Q_R to the convective heating for
625 the October MJO was 18%, approaching the 20% threshold proposed for radiative-
626 convective instability (Yu et al. 1998; Lee et al. 2001; Lin and Mapes 2004; Jiang et al.
627 2011). However, the ratio for the November MJO was far less, 11%, highlighting yet
628 another distinction between the two DYNAMO MJOs.

629 In addition to the budget analyses presented herein, large-scale forcing fields (e.g., Wu
630 et al. 2000) have been computed and made available for application to cloud-resolving and
631 single-column models. The good agreement between budget integral constraints (i.e., rainfall,
632 $\langle Q_R \rangle$, surface fluxes) lends confidence to the accuracy of the forcing fields and their ability
633 to capture the large-scale signal associated with the MJO. The forcing data sets used in this
634 study are available from the National Center for Atmospheric Research Earth Observation
635 Laboratory DYNAMO archive (http://data.eol.ucar.edu/master_list/?project=DYNAMO).

636 Although the above results have yielded insight into the convective heating profiles and
637 inferences regarding cloud populations in the DYNAMO MJOs, further work is needed to
638 directly relate these findings to the research radar observations of precipitation systems at
639 the S-PolKa site on Gan Island, the TOGA radar on the R/V *Revelle*, and the 5-cm radar
640 on the R/V *Mirai*, as well as cloud radar observations on Gan Island. This work is currently
641 underway. In addition, we have not explored in this study the diurnal cycle of convection,
642 which turns out to be particularly important during the suppressed phases of the MJOs. A
643 companion paper on this topic is in preparation.

644 *Acknowledgments.*

645 This research has been supported by the National Science Foundation under Grants
646 AGS-1059899, AGS-1138353, and AGS-1360237, the National Aeronautics and Space Ad-
647 ministration under Grant NNX13AF74G, and Department of Energy Grant DE-SC0008582.
648 We thank Zhe Feng of PNNL for generously providing the radiative heating rates for Gan
649 Island, Wayne Schubert for helpful discussions, and Rick Taft for assistance with preparation
650 of figures.

REFERENCES

- 653 Adler, R. F., et al., 2003: The Version 2 Global Precipitation Climatology Project (GPCP)
654 monthly precipitation analysis (1979-present). *J. Hydrometeor.*, **4**, 1147–1167.
- 655 Ao, C. O., T. K. Meehan, G. A. Hajj, A. J. Mannucci, and G. Beyerle, 2003: Lower-
656 tropospheric refractivity bias in GPS occultation retrievals. *J. Geophys. Res.*, **48**, doi:
657 10.1029/2002JD003216.
- 658 Aonashi, K., et al., 2009: GSMaP passive, microwave precipitation retrieval algorithm:
659 Algorithm description and validation. *J. Meteor. Soc. Japan*, **87A**, 119–136.
- 660 Benedict, J. and D. A. Randall, 2007: Observed characteristics of the MJO relative to
661 maximum rainfall. *J. Atmos. Sci.*, **64**, 2332–2354.
- 662 Chikira, M., 2014: Easward-propagating intraseasonal oscillation represented by Chikira-
663 Sugiyama cumulus parameterization. Part II: Understanding moisture variation under
664 weak temperature gradient balance. *J. Atmos. Sci.*, **71**, 615–639.
- 665 Ciesielski, P. E., L. Hartten, and R. H. Johnson, 1997: Impacts of merging profiler and
666 rawinsonde winds on TOGA COARE analyses. *J. Atmos. Oceanic Technol.*, **14**, 1264–
667 1279.
- 668 Ciesielski, P. E., R. H. Johnson, P. T. Haertel, and J. Wang, 2003: Corrected TOGA COARE
669 sounding humidity data: Impact on diagnosed properties of convection and climate over
670 the warm pool. *J. Climate*, **16**, 2370–2384.
- 671 Ciesielski, P. E., R. H. Johnson, K. Yoneyama, and R. K. Taft, 2014b: Mitigation of Sri Lanka
672 island effects in Colombo sounding data its impact on DYNAMO analyses. *J. Meteor. Soc.*
673 *Japan*, (in press).

674 Ciesielski, P. E., et al., 2014a: Quality controlled upper-air sounding dataset for DY-
675 NAMO/CINDY/AMIE: Development and corrections. *J. Atmos. Oceanic Technol.*, **31**,
676 741–764.

677 Del Genio, A. D., Y. Chen, D. Kim, and M.-S. Yao, 2012: The MJO transition from shallow
678 to deep convection in *cloudsat*/CALIPSO and GISS GCM simulations. *J. Climate*, **25**,
679 3755–3770.

680 Emanuel, K. A. and M. Bister, 1996: Moist convective velocity and buoyancy scales. *J.*
681 *Atmos. Sci.*, **53**, 3276–3285.

682 Fairall, C. W., E. F. Bradley, D. P. Rogers, J. B. Edson, and G. S. Young, 1996: Bulk
683 parameterization of air-sea fluxes for TOGA COARE. *J. Geophys. Res.*, **101**, 3747–3764.

684 Feng, Z., S. A. McFarlane, C. Schumacher, S. Ellis, and N. Bharadwaj, 2014: Constructing a
685 merged cloud-precipitation radar dataset for tropical clouds during the DYNAMO/AMIE
686 experiment on Addu Atoll. *J. Atmos. Oceanic Technol.*, **31**, 1021–1042.

687 Figa-Saldaña, J., J. J. W. Wilson, E. Attema, R. Gelsthorpe, M. R. Drinkwater, and A. Stof-
688 felen, 2002: The advanced scatterometer (ASCAT) on the meteorological operational
689 (MetOp) platform: A follow on for European wind scatterometers. *Can. J. Remote Sens-*
690 *ing*, **28**, 404–412.

691 Funk, A., C. Schumacher, and J. Awaka, 2013: Analysis of rain classifications over the tropics
692 by Version 7 of the TRMM PR 2A23 algorithm. *J. Meteor. Soc. Japan*, **91**, 257–272.

693 Gosnell, R., C. W. Fairall, and P. J. Webster, 1995: The sensible heat of rainfall in the
694 tropical ocean. *J. Geophys. Res.*, **100**, 18 437–18 442.

695 Gottschalck, J., P. E. Roundy, C. J. S. III, A. Vintzileos, and C. Zhang, 2013: Large-scale
696 atmospheric and oceanic conditions during the 2011-12 DYNAMO field campaign. *Mon.*
697 *Wea. Rev.*, **141**, 4173–4196.

698 Haertel, P. T., G. N. Kiladis, A. Denno, and T. M. Rickenbach, 2008: Vertical-mode decom-
699 positions of 2-day waves and the Madden-Julian Oscillation. *J. Atmos. Sci.*, **65**, 813–833.

700 Hartmann, D. L., H. H. Hendon, and R. A. Houze, Jr., 1984: Some implications of the
701 mesoscale circulations in tropical cloud clusters for large-scale dynamics and climate. *J.*
702 *Atmos. Sci.*, **41**, 113–121.

703 Hartmann, D. L., M. E. Ockert-Bell, and M. L. Michelsen, 1992: The effect of cloud type on
704 the Earth’s energy balance: Global analysis. *J. Climate*, **5**, 1281–1304.

705 Holmlund, K., C. S. Velden, and M. Rohn, 2001: Enhanced automated quality control
706 applied to high-density satellite-derived winds. *Mon. Wea. Rev.*, **129**, 517–529.

707 Huffman, G. J., R. F. Adler, D. T. Bolvin, G. Gu, E. J. Nelkin, K. P. Bowman, E. F.
708 Stocker, and D. B. Wolff, 2007: The TRMM multi-satellite precipitation analysis: Quasi-
709 global, multi-year, combined-sensor precipitation estimates at fine scale. *J. Hydrometeor.*,
710 **8**, 33–55.

711 Hung, M.-P., J.-L. Lin, W. Wang, D. Kim, T. Shinoda, and S. J. Weaver, 2013: MJO and
712 convectively coupled equatorial waves simulated by CMIP5 climate models. *J. Climate*,
713 **26**, 6185–6214.

714 Jiang, X., et al., 2011: Vertical diabatic heating structure of the MJO: Intercomparison
715 between recent reanalyses and TRMM. *Mon. Wea. Rev.*, **139**, 3208–3223.

716 Johnson, R. H., 1980: Diagnosis of convective and mesoscale motions during Phase III of
717 GATE. *J. Atmos. Sci.*, **37**, 733–753.

718 Johnson, R. H. and P. E. Ciesielski, 2000: Rainfall and radiative heating rate estimates from
719 TOGA COARE atmospheric budgets. *J. Atmos. Sci.*, **57**, 1497–1514.

720 Johnson, R. H. and P. E. Ciesielski, 2002: Characteristics of the 1998 summer monsoon
721 onset over the northern South China Sea. *J. Meteor. Soc. Japan*, **80**, 561–578.

- 722 Johnson, R. H. and P. E. Ciesielski, 2013: Structure and properties of Madden-Julian Oscil-
723 lations deduced from DYNAMO sounding arrays. *J. Atmos. Sci.*, **70**, 3157–3179.
- 724 Johnson, R. H. and X. Lin, 1987: Episodic trade wind regimes over the western Pacific warm
725 pool. *J. Atmos. Sci.*, **54**, 2020–2034.
- 726 Johnson, R. H., T. M. Rickenbach, S. A. Rutledge, P. E. Ciesielski, and W. H. Schubert,
727 1999: Trimodal characteristics of tropical convection. *J. Atmos. Sci.*, **58**, 2729–2750.
- 728 Joyce, R. J., J. E. Janowiak, P. A. Arkin, and P. Xie, 2004: A method that produces
729 global precipitation estimates from passive microwave and infrared data at high spatial
730 and temporal resolution. *J. Hydrometeor.*, **5**, 487–503.
- 731 Katsumata, M., P. E. Ciesielski, and R. H. Johnson, 2011: Evaluation of budget analysis
732 during MISMO. *J. Appl. Meteor. Climatol.*, **40**, 241–254.
- 733 Kikuchi, K. and Y. N. Takayabu, 2004: The development of organized convection associated
734 with the MJO during TOGA COARE IOP: Trimodal characteristics. *Geophys. Res. Lett.*,
735 **31**, doi:10.1029/2004GL019601.
- 736 Kiladis, G. N., K. H. Straub, and P. T. Haertel, 2005: Zonal and vertical structure of the
737 Madden-Julian oscillation. *J. Atmos. Sci.*, **62**, 2790–2809.
- 738 Kiladis, G. N., K. H. Straub, G. C. Reid, and K. S. Gage, 2001: Aspects of interannual and
739 intraseasonal variability of the tropopause and lower stratosphere. *Quart. J. Roy. Meteor.*
740 *Soc.*, **127**, 1961–1984.
- 741 Kiladis, G. N., M. C. Wheeler, P. T. Haertel, K. H. Straub, and P. E. Roundy, 2009: Con-
742 vectively coupled equatorial waves. *Rev. Geophys.*, **47**, 2003, doi:10.1029/2008RG000266.
- 743 Kubota, T., et al., 2007: Global precipitation map using satellite-borne microwave radiome-
744 ters by the GSMaP project: Production and validation. *IEEE Trans. Geosci. Remote*
745 *Sens.*, **45**, 2259–2275.

746 Kumar, B. P., J. Vialard, M. Lengaigne, V. S. N. Murty, and M. J. McPhaden, 2012:
747 TropFlux: Air-sea fluxes for the global tropical oceans - Description and evaluation. *Clim.*
748 *Dynam.*, **38**, 1521–1543.

749 Kuo, Y.-H., T.-K. Lee, S. Sokolovskiy, C. Rocken, W. Schreiner, D. Hunt, and R. A. Anthes,
750 2004: Inversion and error estimation of GPS radio occultation data. *J. Meteor. Soc. Japan*,
751 **82**, 507–531.

752 L’Ecuyer, T. S. and G. McGarragh, 2010: A 10-year climatology of tropical radiative heating
753 and its vertical structure from TRMM observations. *J. Climate*, **23**, 519–541.

754 Lee, M.-I., I.-S. Kang, J.-K. Kim, and B. E. Mapes, 2001: Influence of cloud-radiation
755 interaction on simulating tropical intraseasonal oscillation with an atmosphere general
756 circulation model. *J. Geophys. Res.*, **106**, 14,291–14,233.

757 Lin, J.-L. and B. E. Mapes, 2004: Radiation budget of the tropical intraseasonal oscillation.
758 *J. Atmos. Sci.*, **61**, 2050–2062.

759 Lin, J.-L., B. E. Mapes, M. Zhang, and N. Newman, 2004: Stratiform precipitation, vertical
760 heating profiles, and the Madden-Julian Oscillation. *J. Atmos. Sci.*, **61**, 296–309.

761 Lin, X. and R. H. Johnson, 1996: Heating, moistening, and rainfall over the western Pacific
762 warm pool during TOGA COARE. *J. Atmos. Sci.*, **53**, 3367–3383.

763 Luo, H. and M. Yanai, 1984: The large-scale circulation and heat sources over the Tibetan
764 Plateau and surrounding areas during the early summer of 1979. part ii: Heat and moisture
765 budgets. *Mon. Wea. Rev.*, **112**, 966–989.

766 Madden, R. A. and P. R. Julian, 1972: Description of global-scale circulation cells in the
767 tropics with a 40-50 day period. *J. Atmos. Sci.*, **29**, 1109–1123.

768 Mapes, B. E., P. E. Ciesielski, and R. H. Johnson, 2003: Sampling errors in rawinsonde-array
769 budgets. *J. Atmos. Sci.*, **60**, 2697–2714.

770 Mapes, B. E., S. Tulich, J. Lin, and P. Zuidema, 2006: The mesoscale convection life cycle:
771 Building block or prototype for large-scale tropical waves? *Dyn. Atmos. Oceans*, **42**, 3–29.

772 McNab, A. L. and A. K. Betts, 1978: Mesoscale budget study of cumulus convection. *Mon.*
773 *Wea. Rev.*, **106**, 1317–1331.

774 Ooyama, K., 1990: A thermodynamic foundation for modeling the moist atmosphere. *J.*
775 *Atmos. Sci.*, **47**, 2580–2593.

776 Randall, D. A., Harshvardhan, D. A. Dazlich, and T. G. Corsetti, 1989: Interactions among
777 radiation, convection, and large-scale dynamics in a general circulation model. *J. Atmos.*
778 *Sci.*, **46**, 1943–1970.

779 Raymond, D. J., 2000: The Hadley circulation as a radiative-convective instability. *J. Atmos.*
780 *Sci.*, **57**, 1286–1297.

781 Raymond, D. J., 2001: A new model of the Madden-Julian oscillation. *J. Atmos. Sci.*, **58**,
782 2807–2819.

783 Schumacher, C. and R. A. Houze, Jr., 2003: Stratiform rain in the tropics as seen by the
784 TRMM Precipitation Radar. *J. Climate*, **16**, 1739–1756.

785 Sherwood, S. C., V. Ramanathan, T. P. Barnett, M. K. Tyree, and E. Roeckner, 1994: Re-
786 sponse of an atmospheric general circulation model to radiative forcing of tropical clouds.
787 *J. Geophys. Res.*, **99**, 20 829–20 845.

788 Slingo, A. and J. M. Slingo, 1988: The response of a general circulation model to cloud
789 longwave radiative forcing. I: Introduction and initial experiments. *Quart. J. Roy. Meteor.*
790 *Soc.*, **114**, 1027–1962.

791 Slingo, A. and J. M. Slingo, 1991: The response of a general circulation model to cloud
792 longwave radiative forcing. II: Further studies. *Quart. J. Roy. Meteor. Soc.*, **117**, 333–
793 364.

794 Sobel, A., S. Wang, and D. Kim, 2014: Moist static energy budget of the MJO during
795 DYNAMO. *J. Atmos. Sci.*, (in press).

796 Stephens, G. L., M. J. Webb, P. J. Minnett, P. H. Daum, L. Kleinman, I. Wittmeyer,
797 and D. A. Randall, 1994: Observations of the Earth's radiation budget in relation to
798 atmospheric hydrology. 4: Atmospheric column radiative cooling over the world's oceans.
799 *J. Geophys. Res.*, **99**, 18,585–18,604.

800 Stephens, G. L., P. J. Webster, R. H. Johnson, R. Engelen, and T. S. L'Ecuyer, 2004:
801 Observational evidence for the mutual regulation of the tropical hydrological cycle and
802 the tropical sea surface temperatures. *J. Climate*, **17**, 2213–2224.

803 Tao, W.-K., C.-L. Shie, D. Johnson, S. Braun, R. H. Johnson, and P. E. Ciesielski, 2003:
804 Convective systems over the South China Sea: Cloud-resolving model simulations. *J.*
805 *Atmos. Sci.*, **60**, 2929–2956.

806 Trenberth, K. E., 1991: Climate diagnostics from global analyses: Conservation of mass in
807 ECMWF analyses. *J. Climate*, **4**, 707–722.

808 Tung, W.-W., C. Lin, B. Chen, M. Yanai, and A. Arakawa, 1999: Basic modes of cumulus
809 heating and drying observed during TOGA-COARE IOP. *Geophys. Res. Lett.*, **26**, 3117–
810 3120.

811 Virts, K. S. and J. M. Wallace, 2010: Annual, interannual, and intraseasonal variability of
812 tropical tropopause transition layer cirrus. *J. Atmos. Sci.*, **67**, 3113–3129.

813 Virts, K. S., J. M. Wallace, Q. Fu, and T. P. Ackerman, 2010: Tropical tropopause transition
814 layer cirrus as represented by calipso lidar observations. *J. Atmos. Sci.*, **67**, 3097–3112.

815 Wang, J., H. L. Cole, D. J. Carlson, E. R. Miller, K. Beierle, A. Paukkunen, and T. K. Laine,
816 2002: Corrections of the humidity measurement errors from the vaisala rs80 radiosonde–
817 Application to TOGA COARE data. *J. Atmos. Oceanic Technol.*, **19**, 981–1002.

818 Webster, P. J., 1994: TOGA COARE: The role of hydrological processes in ocean-atmosphere
819 interaction. *Rev. Geophys.*, **32**, 427–476.

820 Webster, P. J. and R. Lukas, 1992: TOGA COARE: The coupled ocean-atmosphere response
821 experiment. *Bull. Amer. Meteor. Soc.*, **73**, 1377–1416.

822 Weller, R. A. and S. P. Anderson, 1996: Surface meteorology and air-sea fluxes in the western
823 equatorial Pacific warm pool during the TOGA Coupled Ocean-Atmosphere Response
824 Experiment. *J. Climate*, **9**, 1959–1990.

825 Wheeler, M. C. and H. H. Hendon, 2004: An all-season real-time multivariate MJO index:
826 Development of an index for monitoring and prediction. *Mon. Wea. Rev.*, **132**, 1917–1932.

827 Wielicki, B. A., B. R. Barkstrom, E. F. Harrison, R. B. Lee, III, G. L. Smith, and J. E.
828 Cooper, 1996: Clouds and the earth’s radiant energy system (CERES): An earth observing
829 system experiment. *Bull. Amer. Meteor. Soc.*, **77**, 853–868.

830 Wu, X., M. W. Moncrieff, and K. A. Emanuel, 2000: Evaluation of large-scale forcing during
831 TOGA COARE for cloud-resolving models and single-column models. *J. Atmos. Sci.*, **57**,
832 2977–2985.

833 Yanai, M., S. Esbensen, and J.-H. Chu, 1973: Determination of bulk properties of tropical
834 cloud clusters from large-scale heat and moisture budgets. *J. Atmos. Sci.*, **30**, 611–627.

835 Yanai, M. and R. H. Johnson, 1993: Impacts of cumulus convection on thermodynamic fields.
836 *The representation of cumulus convection in numerical models*, Amer. Meteor. Soc., No. 46
837 in Meteor. Monogr., 39–62.

838 Yoneyama, K., C. Zhang, and C. N. Long, 2013: Tracking pulses of the Madden-Julian
839 Oscillation. *Bull. Amer. Meteor. Soc.*, **94**, 1871–1891.

840 Yoneyama, K., et al., 2008: MISMO field experiment in the equatorial Indian Ocean. *Bull.*
841 *Amer. Meteor. Soc.*, **89**, 1889–1903.

- 842 Yu, J.-Y., C. Chou, and J. D. Neelin, 1998: Estimating the gross moist stability of the
843 tropical atmosphere. *J. Atmos. Sci.*, **55**, 1354–1372.
- 844 Yu, L. and R. A. Weller, 2007: Objectively analyzed air-sea heat fluxes for the global oceans
845 (1981-2005). *Bull. Amer. Meteor. Soc.*, **88**, 527–539.
- 846 Zhang, C., 2005: Madden-Julian Oscillation. *Rev. Geophys.*, **89**, 2003, doi:10.1029/
847 2004RG000158.
- 848 Zhang, C., 2013: The Madden-Julian Oscillation: Bridging weather and climate. *Bull. Amer.*
849 *Meteor. Soc.*, **94**, 1849–1870.
- 850 Zhang, C., J. Gottschalck, E. D. Maloney, M. W. Moncrieff, F. Vitart, D. E. Waliser,
851 B. Wang, and M. C. Wheeler, 2013: Cracking the MJO nut. *Geophys. Res. Lett.*, **40**,
852 1223–1230, doi:10.1002/grl.50244,2013.
- 853 Zuluaga, M. D. and R. A. Houze, Jr., 2013: Evolution of the population of precipitating
854 convective systems over the Equatorial Indian Ocean in active phases of the Madden-
855 Julian Oscillation. *J. Atmos. Sci.*, **70**, 2713–2725.

856 **List of Tables**

857 1 SOP-mean rainfall and radiative heating rates based on budgets and satellite
858 estimates for DYNAMO NSA and SSA, as well as comparisons with four-
859 month budget averages for TOGA COARE Intensive Flux Array (IFA). Areas
860 of arrays are also indicated. 37

TABLE 1. SOP-mean rainfall and radiative heating rates based on budgets and satellite estimates for DYNAMO NSA and SSA, as well as comparisons with four-month budget averages for TOGA COARE Intensive Flux Array (IFA). Areas of arrays are also indicated.

Item	Source	DYNAMO NSA	DYNAMO SSA	COARE IFA
Areas		(700 km) ²	(830 km) ²	(474 km) ²
Rainfall rates (mm day ⁻¹)				
	Q_2 budget	9.2	10.4	8.4
	TRMM	8.7	9.0	
	CMORPH	9.1	9.6	
	GPCP	9.7	9.1	
	GSMaP	9.1	8.1	
Tropospheric-mean radiative heating $\langle Q_R \rangle$ (K day ⁻¹)				
	Budgets without rain correction	-0.53	-0.46	
	Budgets with rain correction	-0.59	-0.53	-0.55
	CERES	-0.63	-0.62	

List of Figures

- 861
- 862 1 DYNAMO/CINDY/AMIE sounding network for the period October-December
863 2011. Analysis domain includes high-frequency soundings (4 and 8 per day;
864 yellow and red dots, respectively) and operational sounding sites (1 or 2 per
865 day; black dots). Data from R/V *Sagar Kanya* (*S. K.*) and R/V *Baruna Jaya*
866 (*B. J.*), which were on station for brief periods (25 September-19 October for
867 *S. K.* and 5-18 December for *B. J.*), were also utilized in the analyses. Sites
868 with enhanced sounding frequency during the Special Observing Period are
869 labeled. 42
- 870 2 (Upper three panels) Time series of daily-averaged sensible and latent heat
871 fluxes (W m^{-2}), and SST ($^{\circ}\text{C}$) from TropFlux (black curves) and the R/V
872 *Revelle* (red pluses). (Lower panel) Average rainfall rate (mm day^{-1}) within
873 a 1° radius of *Revelle* from TRMM 3B42. Mean values for TropFlux (black)
874 and the *Revelle* (red) are in parentheses. 43
- 875 3 Time-longitude plot of rainfall rates from TRMM 3B42 (3-hourly values,
876 color) and moisture budget (3-day running mean filtering of daily-average
877 values, contours) (mm day^{-1}) averaged 5°N to 5°S for DYNAMO SOP. Ver-
878 tical dashed line denotes center of sounding arrays. Missing moisture budget
879 results between 95 and 100°E marks location of Sumatra, where surface flux
880 data do not exist. 44
- 881 4 Mean rainfall rate (mm day^{-1}) over Indian Ocean for October-November 2011
882 from (upper) TRMM 3B42 product and (lower) moisture budget. White lines
883 denote sounding arrays. Budget rainfall not computed over land due to the
884 absence of surface flux data there. 45

885	5	Time series for October and November of daily-average values of (upper)	
886		apparent heat source Q_1 (K day^{-1}), (middle) apparent moisture sink Q_2 ,	
887		and (lower) TRMM 3B42v7 rainfall rate (mm day^{-1}) for NSA. Wheeler and	
888		Hendon (2004) RMM index shown at bottom. Shaded bar denotes port call	
889		period for R/V <i>Revelle</i> .	46
890	6	As in Fig. 5, except for SSA. Dark and light vertical shaded bars indicate	
891		times when R/V <i>Mirai</i> and <i>Revelle</i> , respectively, were off station.	47
892	7	(left and center panels) Frequency-altitude distributions and (right panel)	
893		SOP-mean profiles of Q_1 and Q_2 for (top) NSA and (bottom) SSA for October-	
894		November 2011.	48
895	8	SOP time series (filtered, 3-day running mean) for NSA of (upper) rainfall rate	
896		(mm day^{-1}) computed from Q_2 budget with (green curve) and without (red	
897		curve) inclusion of ECMWF OA, with comparison to TRMM 3B42v7 data	
898		(black curve); and (lower) changes to Q_2 budget resulting from inclusion of	
899		model reanalyses. Note difference in vertical scale in the two plots. Numbers	
900		in parentheses refer to SOP-mean rainfall rate. Shading denotes period of	
901		R/V <i>Revelle</i> port call.	49
902	9	SOP time series of 3-day running mean filtered rainfall rate (mm day^{-1}) com-	
903		puted from Q_2 budget compared to TRMM 3B42v7, CMORPH, GPCP, and	
904		GSMaP estimates for (upper) NSA and (lower) SSA. Numbers in parentheses	
905		refer to SOP-mean rainfall rates. Light (dark) shading denotes periods of R/V	
906		<i>Revelle</i> (<i>Mirai</i>) port calls.	50
907	10	(left) Time series of net radiative heating rate (K day^{-1}) at Gan Island from	
908		PNNL CombRet product and (right) mean profiles of shortwave (SW), long-	
909		wave (LW) and net radiative heating rates for October-December 2011.	51

- 910 11 SOP time series (3-day running mean filtered, daily-average values) of net
911 radiative heating rate (K day^{-1}) from budgets and CERES product for array
912 areas, and from PNNL CombRet product for Gan Island, for (upper) NSA and
913 (lower) SSA. Thick (thin) black curves are $\langle Q_R \rangle$ with (without) inclusion
914 of terms involving the effects of rain (see text). Numbers in parentheses
915 are SOP-mean values. Light (dark) shading denotes periods of R/V *Revelle*
916 (*Mirai*) port calls. 52
- 917 12 October 1 – December 7 time series (3-day running mean filtered, daily-
918 average values) of (upper) relative humidity (% , with respect to ice for $T < 0$
919 C); (middle) $\langle Q_R \rangle$ from budgets (black) and CERES (red); and (lower)
920 cloud fractional area from CERES for the following definitions of cloud lay-
921 ers: low ($p > 700$ hPa), med-low ($700 \text{ hPa} > p > 500$ hPa), med-hi (500 hPa
922 $> p > 300$ hPa), and high ($p < 300$ hPa) for NSA. Shaded region denotes
923 period when R/V *Revelle* was off station. 53
- 924 13 (upper) Comparison of anomalies of CERES $\langle Q_R \rangle$ and convective heating
925 $\langle Q_{conv} \rangle$ for NSA for DYNAMO SOP. All time series show 3-day running
926 mean filtered, daily-averaged values. (lower) TRMM 3B42 rainfall rate (mm
927 day^{-1}) time series for NSA. Shaded region denotes period when R/V *Revelle*
928 was off station. 54
- 929 14 Time series of daily-average values of (upper) vertical eddy moist static energy
930 flux F (W m^{-2}) and (lower) TRMM 3B42v7 rainfall rate (mm day^{-1}) for NSA
931 for DYNAMO SOP. Shaded region denotes period when R/V *Revelle* was off
932 station. Wheeler and Hendon (2004) RMM Index shown on lower axis. 55
- 933 15 As in Fig. 14, except for SSA. Dark and light vertical shaded bars indicate
934 times when R/V *Mirai* and *Revelle*, respectively, were off station. 56

935 16 SOP-mean profiles of Q_1 , Q_2 , Q_R , $Q_1 - Q_2 - Q_R$, and F (K day^{-1}) for (up-
936 per) NSA and (lower) SSA. Surface sensible plus latent heat flux (F_0) from
937 TropFlux is indicated by asterisks on bottom axes.

57

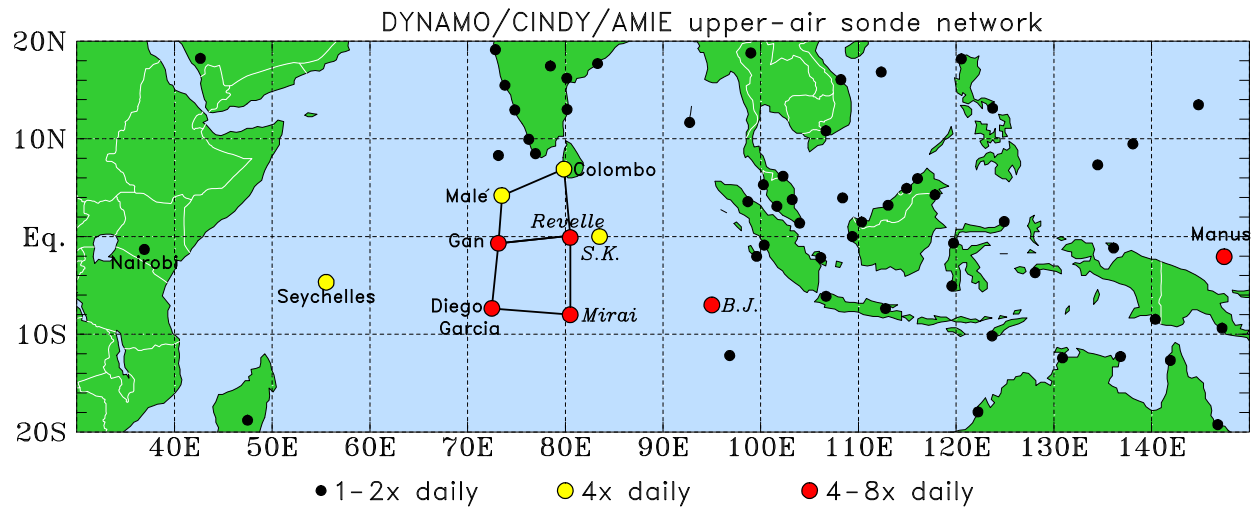


FIG. 1. DYNAMO/CINDY/AMIE sounding network for the period October-December 2011. Analysis domain includes high-frequency soundings (4 and 8 per day; yellow and red dots, respectively) and operational sounding sites (1 or 2 per day; black dots). Data from R/V *Sagar Kanya* (*S. K.*) and R/V *Baruna Jaya* (*B. J.*), which were on station for brief periods (25 September-19 October for *S. K.* and 5-18 December for *B. J.*), were also utilized in the analyses. Sites with enhanced sounding frequency during the Special Observing Period are labeled.

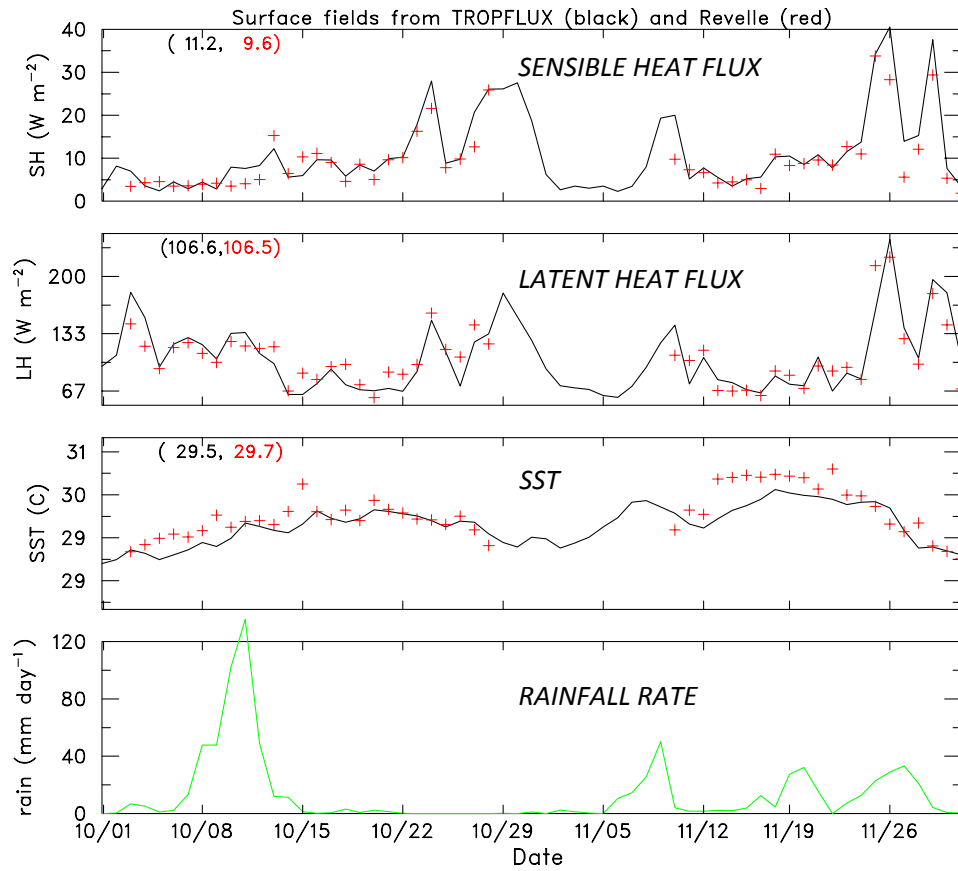


FIG. 2. (Upper three panels) Time series of daily-averaged sensible and latent heat fluxes (W m^{-2}), and SST ($^{\circ}\text{C}$) from TropFlux (black curves) and the R/V *Revelle* (red pluses). (Lower panel) Average rainfall rate (mm day^{-1}) within a 1° radius of *Revelle* from TRMM 3B42. Mean values for TropFlux (black) and the *Revelle* (red) are in parentheses.

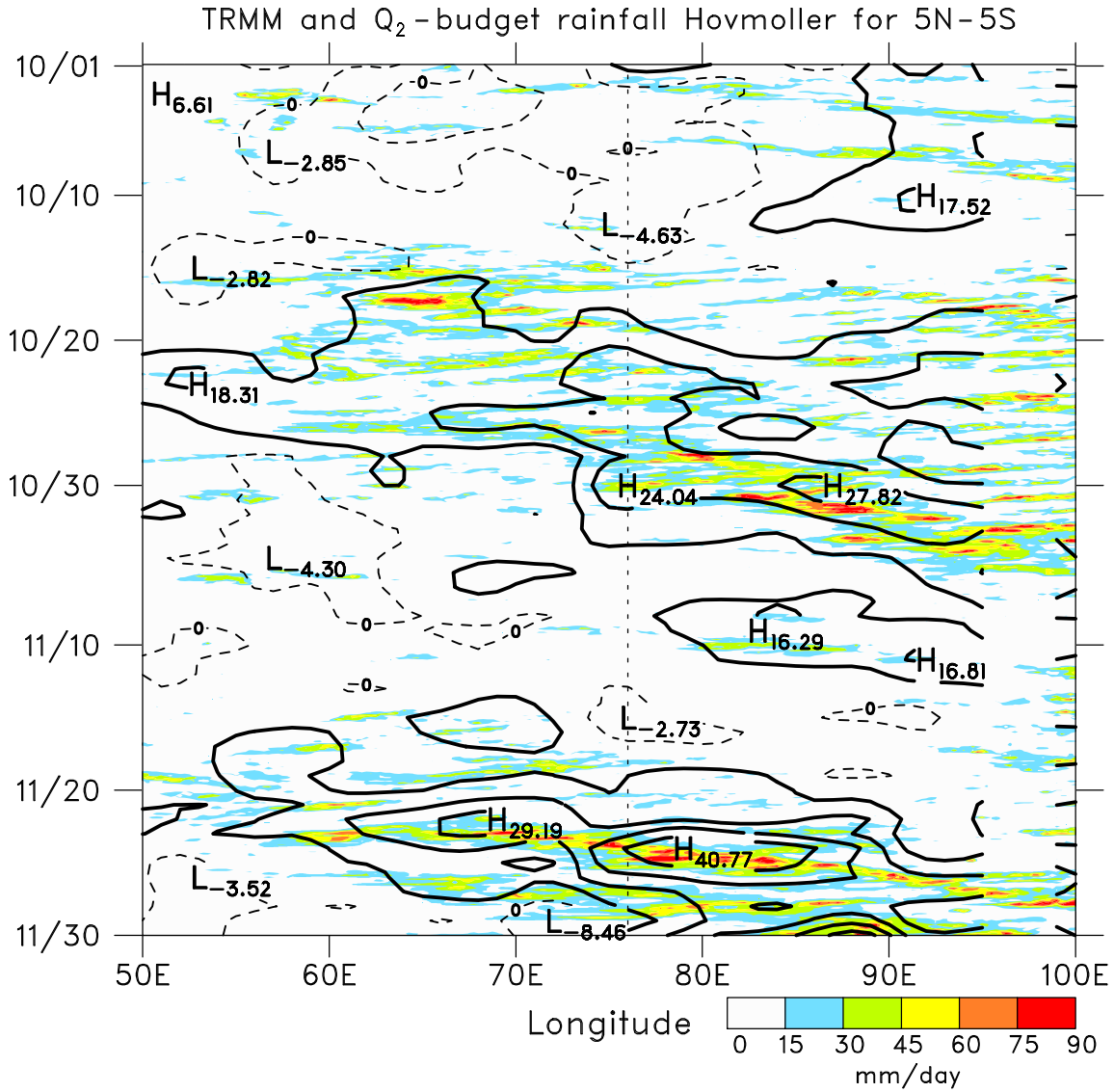


FIG. 3. Time-longitude plot of rainfall rates from TRMM 3B42 (3-hourly values, color) and moisture budget (3-day running mean filtering of daily-average values, contours) (mm day^{-1}) averaged 5°N to 5°S for DYNAMO SOP. Vertical dashed line denotes center of sounding arrays. Missing moisture budget results between 95 and 100°E marks location of Sumatra, where surface flux data do not exist.

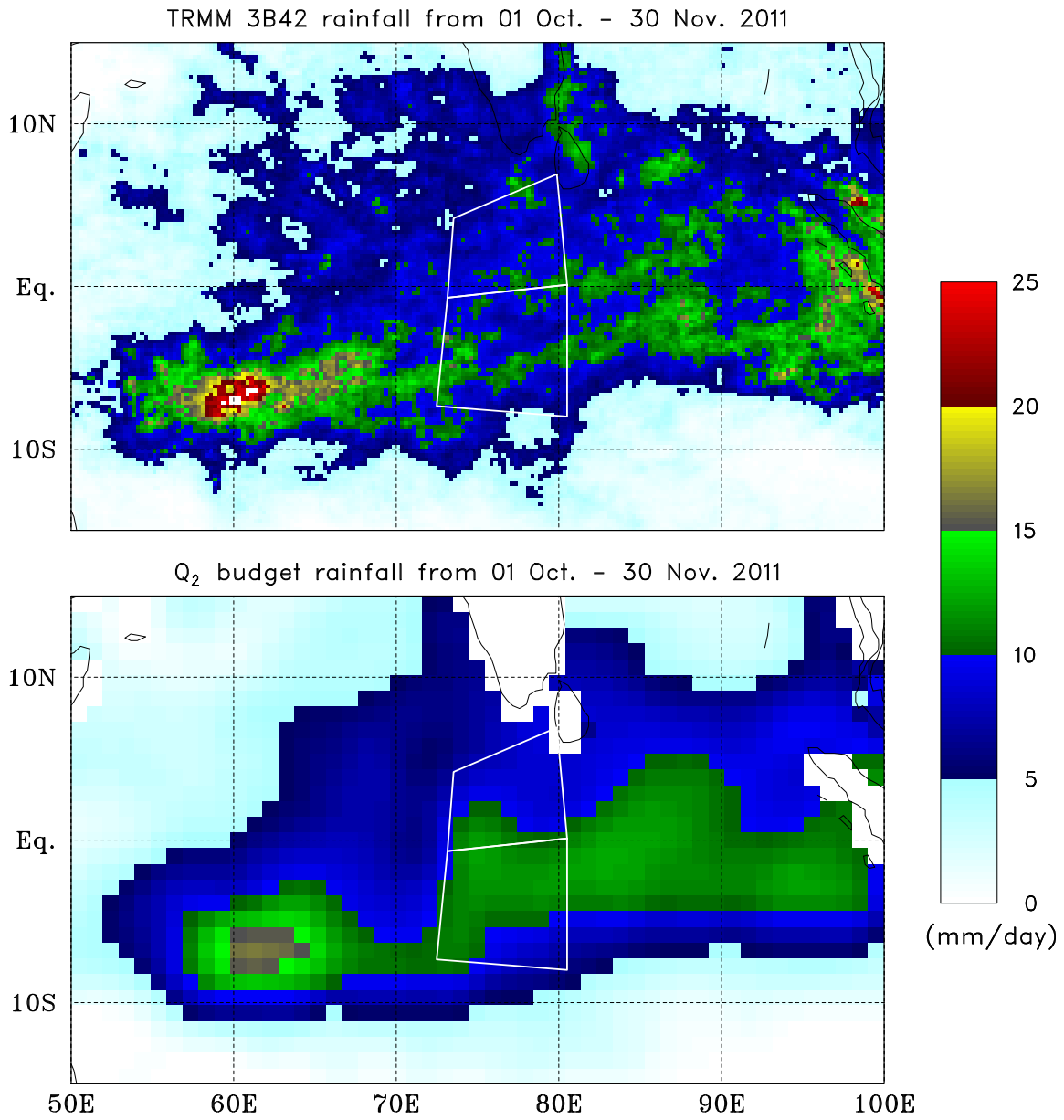


FIG. 4. Mean rainfall rate (mm day^{-1}) over Indian Ocean for October-November 2011 from (upper) TRMM 3B42 product and (lower) moisture budget. White lines denote sounding arrays. Budget rainfall not computed over land due to the absence of surface flux data there.

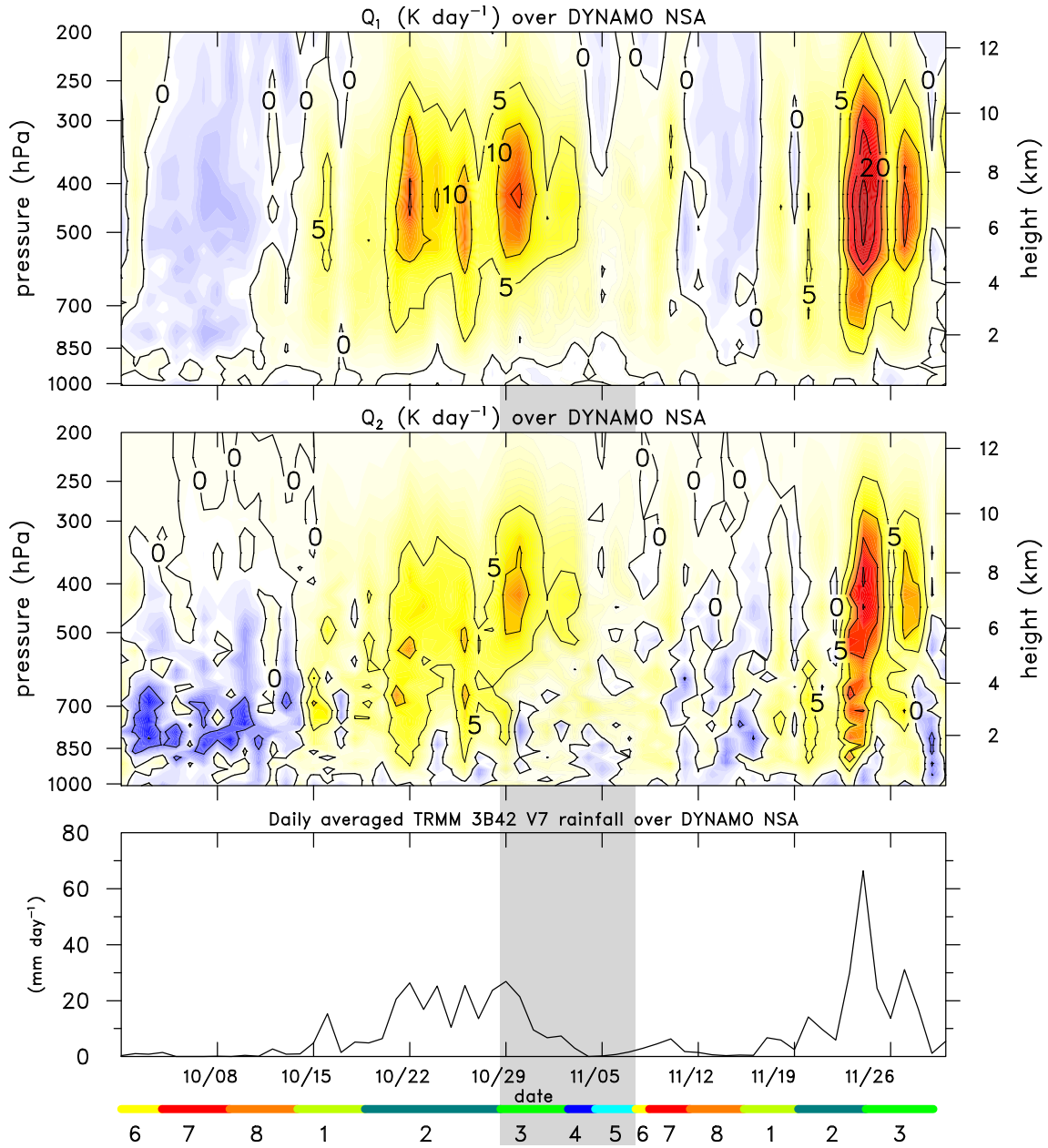


FIG. 5. Time series for October and November of daily-average values of (upper) apparent heat source Q_1 (K day^{-1}), (middle) apparent moisture sink Q_2 , and (lower) TRMM 3B42v7 rainfall rate (mm day^{-1}) for NSA. Wheeler and Hendon (2004) RMM index shown at bottom. Shaded bar denotes port call period for R/V *Revelle*.

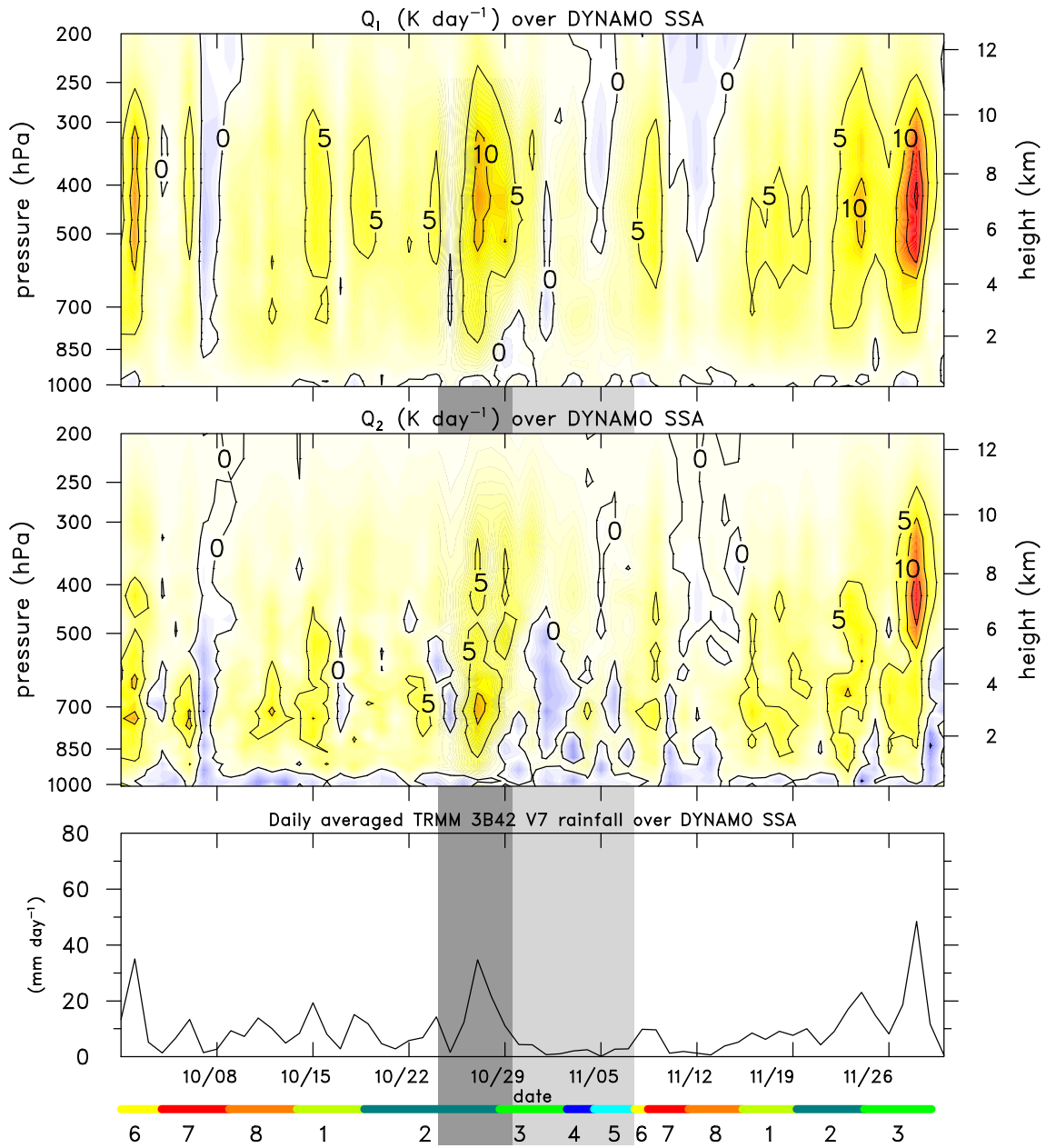


FIG. 6. As in Fig. 5, except for SSA. Dark and light vertical shaded bars indicate times when R/V *Mirai* and *Revelle*, respectively, were off station.

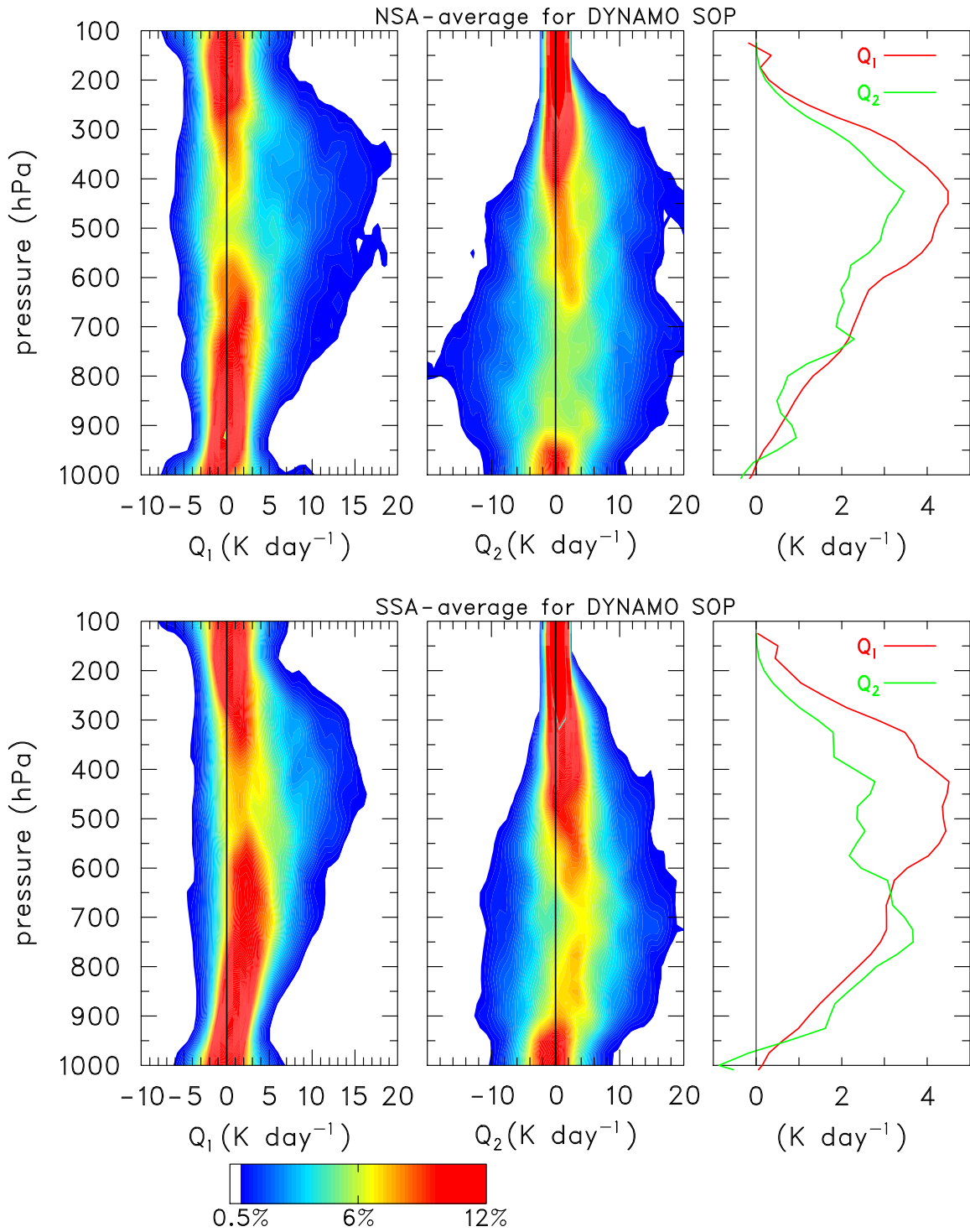


FIG. 7. (left and center panels) Frequency-altitude distributions and (right panel) SOP-mean profiles of Q_1 and Q_2 for (top) NSA and (bottom) SSA for October-November 2011.

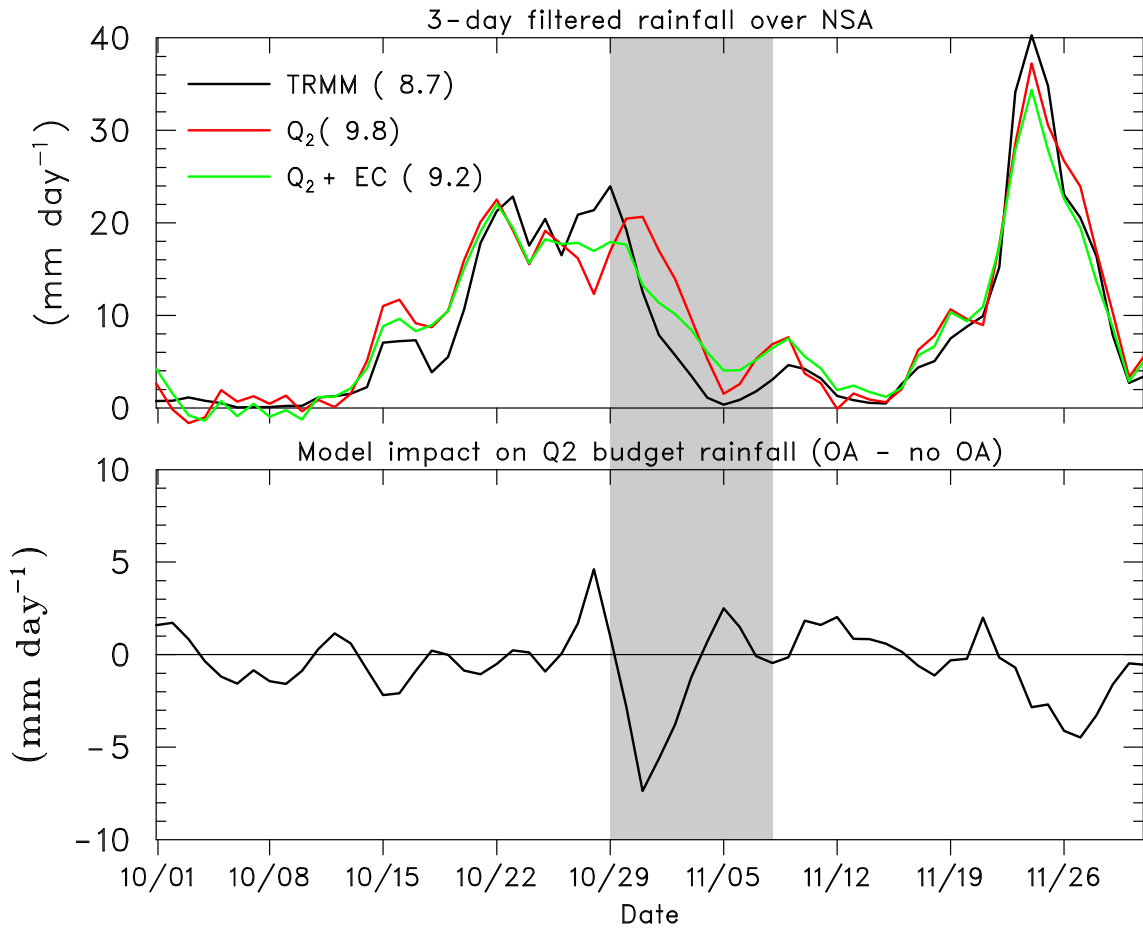


FIG. 8. SOP time series (filtered, 3-day running mean) for NSA of (upper) rainfall rate (mm day^{-1}) computed from Q_2 budget with (green curve) and without (red curve) inclusion of ECMWF OA, with comparison to TRMM 3B42v7 data (black curve); and (lower) changes to Q_2 budget resulting from inclusion of model reanalyses. Note difference in vertical scale in the two plots. Numbers in parentheses refer to SOP-mean rainfall rate. Shading denotes period of R/V *Revelle* port call.

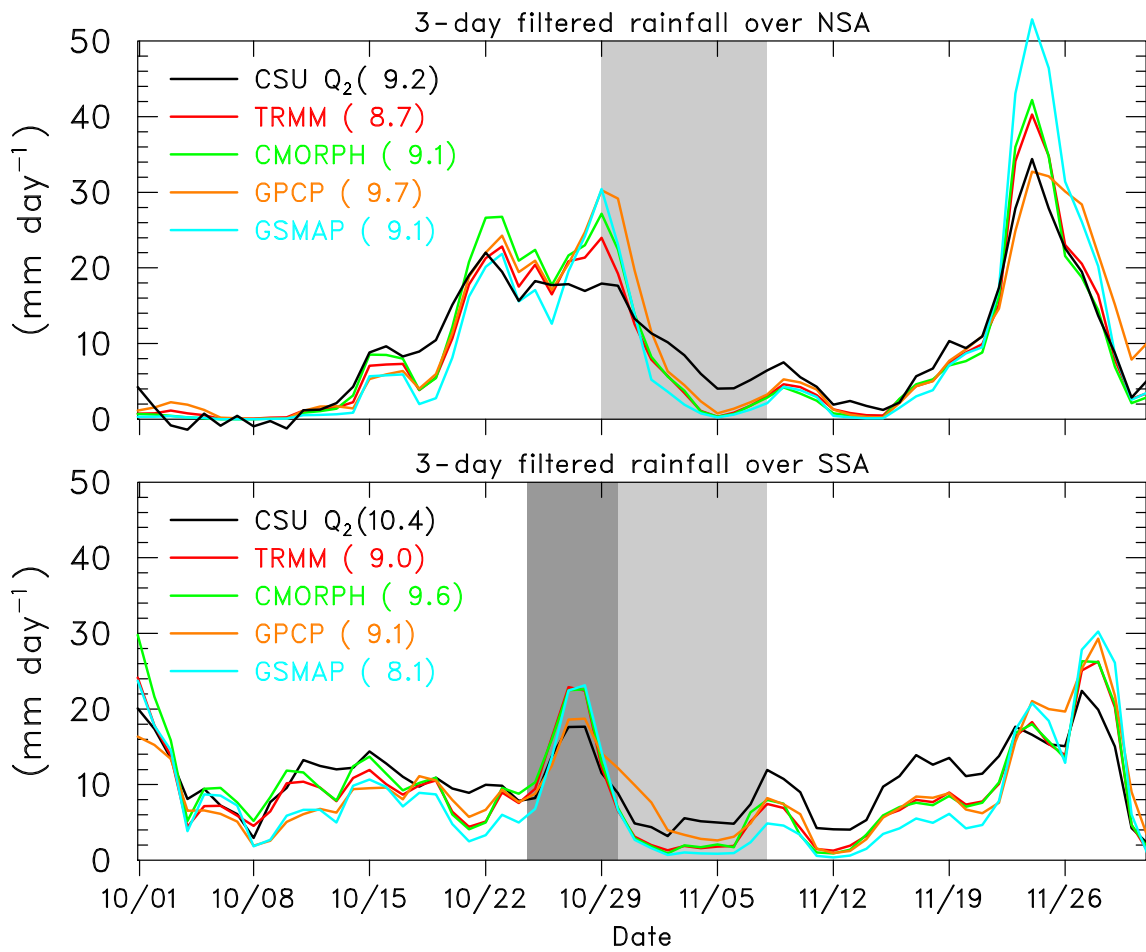


FIG. 9. SOP time series of 3-day running mean filtered rainfall rate (mm day^{-1}) computed from Q_2 budget compared to TRMM 3B42v7, CMORPH, GPCP, and GSMaP estimates for (upper) NSA and (lower) SSA. Numbers in parentheses refer to SOP-mean rainfall rates. Light (dark) shading denotes periods of R/V *Revelle* (*Mirai*) port calls.

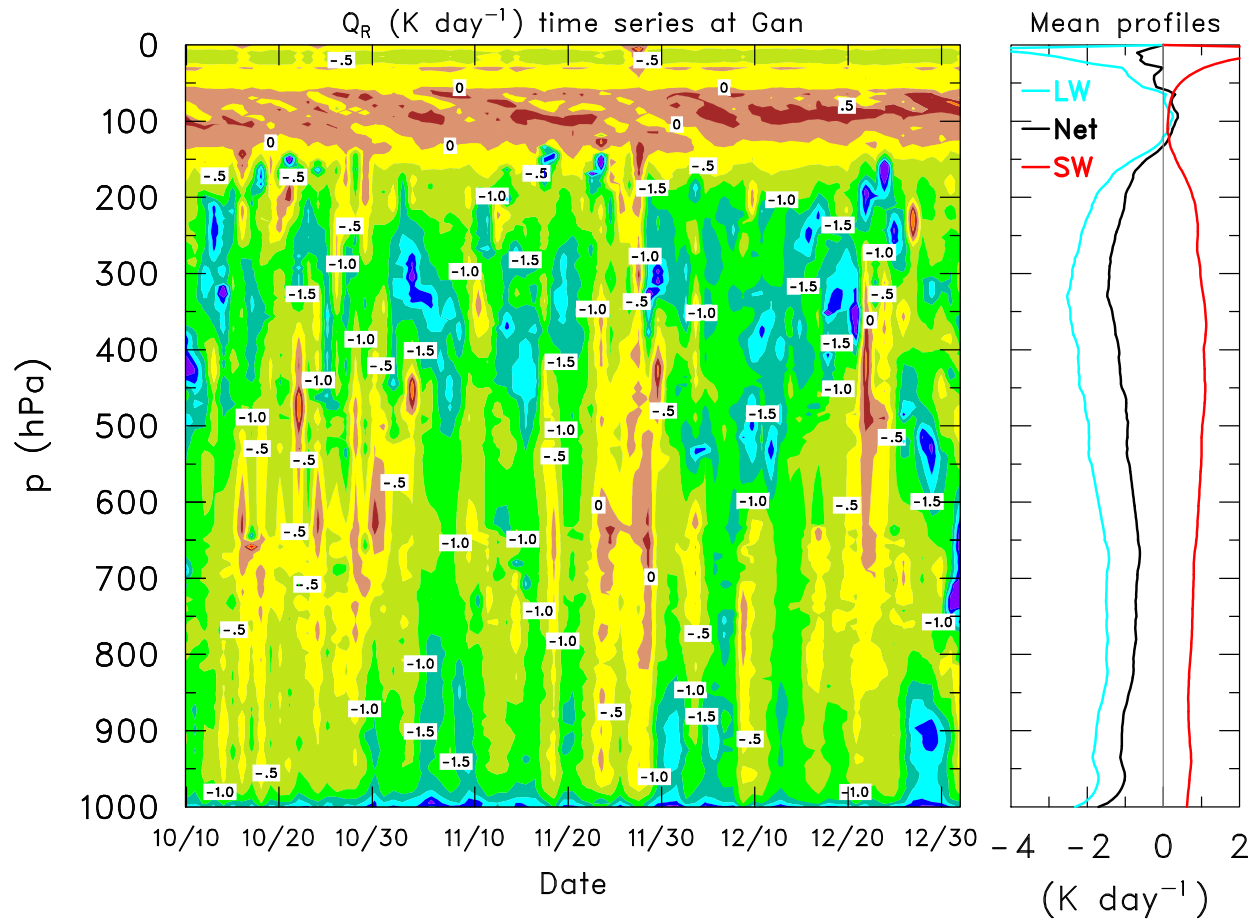


FIG. 10. (left) Time series of net radiative heating rate (K day^{-1}) at Gan Island from PNNL CombRet product and (right) mean profiles of shortwave (SW), longwave (LW) and net radiative heating rates for October-December 2011.

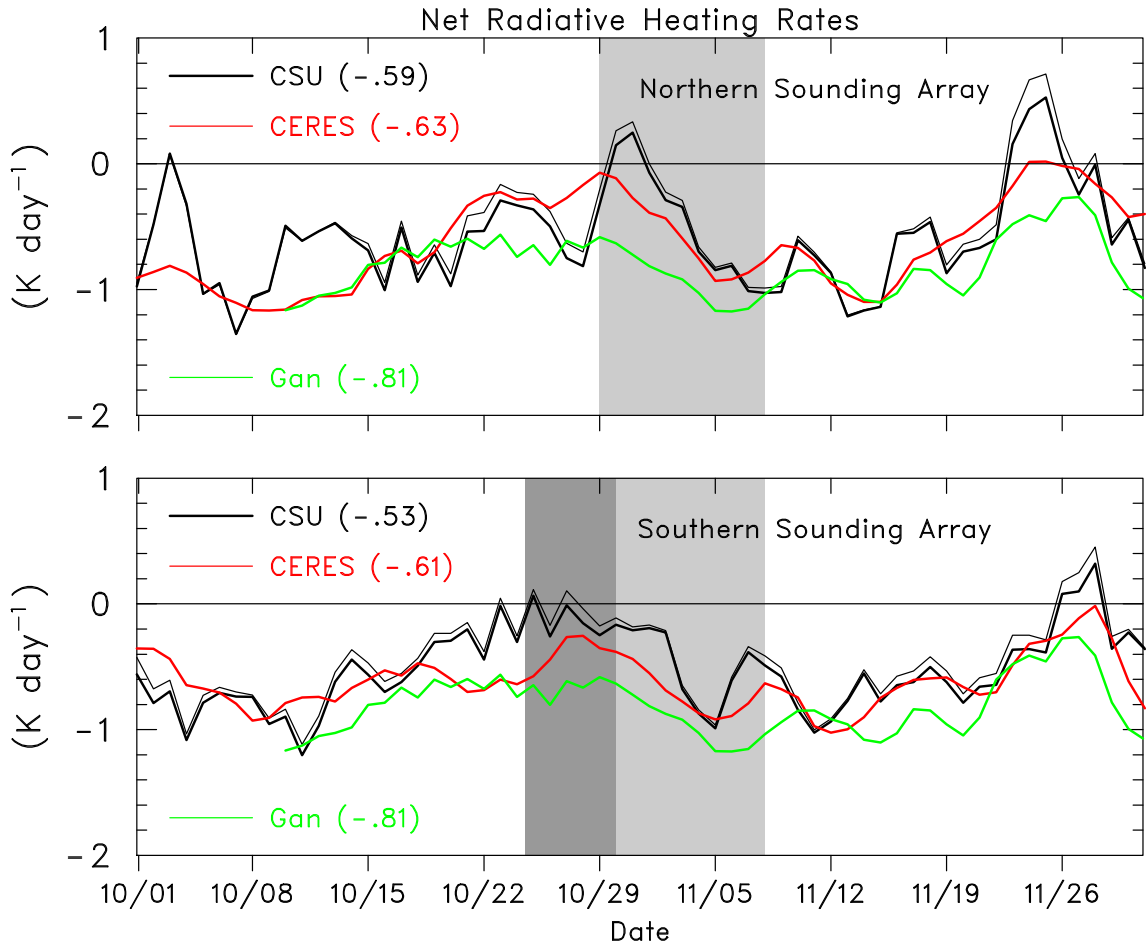


FIG. 11. SOP time series (3-day running mean filtered, daily-average values) of net radiative heating rate (K day^{-1}) from budgets and CERES product for array areas, and from PNNL CombRet product for Gan Island, for (upper) NSA and (lower) SSA. Thick (thin) black curves are $\langle Q_R \rangle$ with (without) inclusion of terms involving the effects of rain (see text). Numbers in parentheses are SOP-mean values. Light (dark) shading denotes periods of R/V *Revelle* (*Mirai*) port calls.

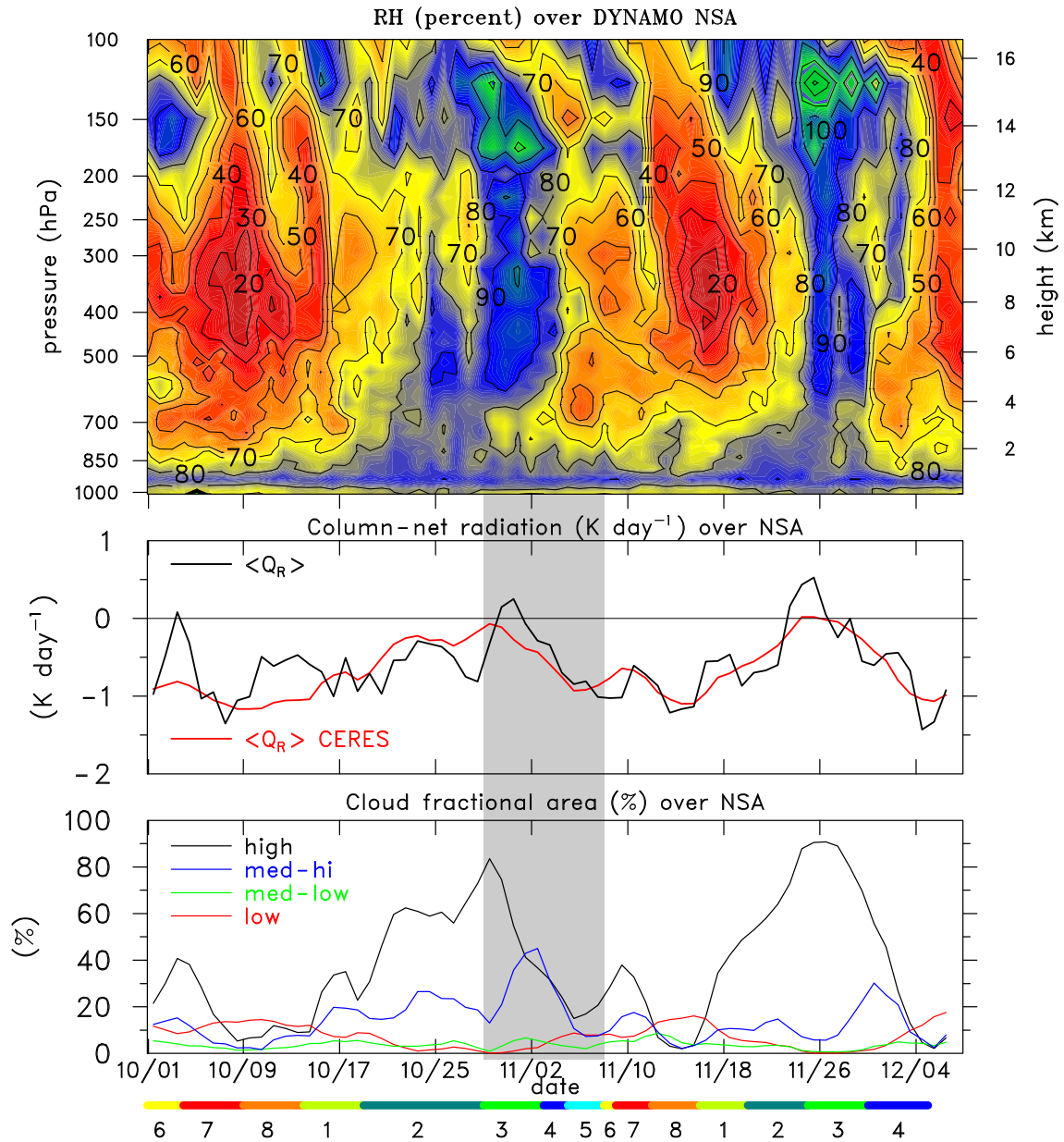


FIG. 12. October 1 – December 7 time series (3-day running mean filtered, daily-average values) of (upper) relative humidity (%; with respect to ice for $T < 0$ C); (middle) $\langle Q_R \rangle$ from budgets (black) and CERES (red); and (lower) cloud fractional area from CERES for the following definitions of cloud layers: low ($p > 700$ hPa), med-low ($700 \text{ hPa} > p > 500$ hPa), med-hi ($500 \text{ hPa} > p > 300$ hPa), and high ($p < 300$ hPa) for NSA. Shaded region denotes period when R/V *Reville* was off station.

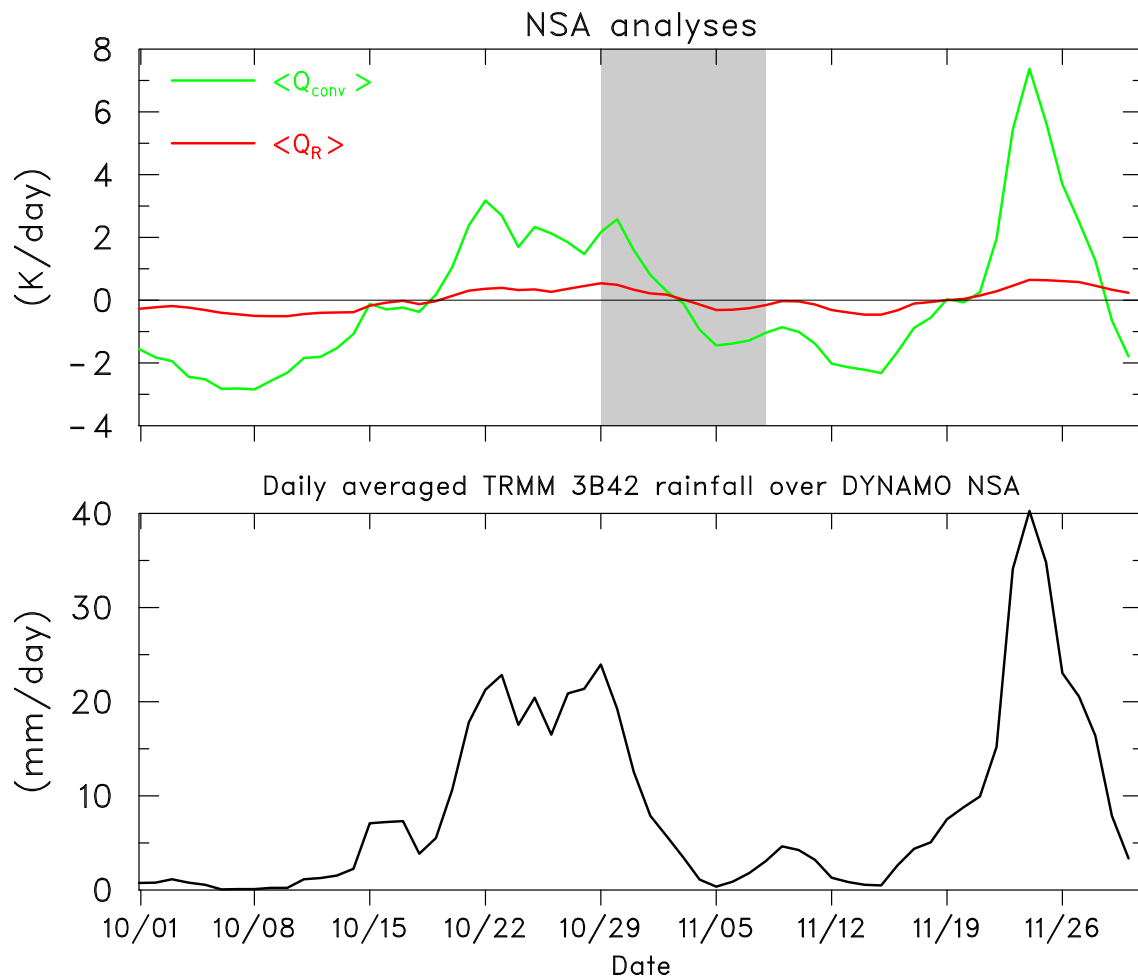


FIG. 13. (upper) Comparison of anomalies of CERES $\langle Q_R \rangle$ and convective heating $\langle Q_{conv} \rangle$ for NSA for DYNAMO SOP. All time series show 3-day running mean filtered, daily-averaged values. (lower) TRMM 3B42 rainfall rate (mm day^{-1}) time series for NSA. Shaded region denotes period when R/V *Revelle* was off station.

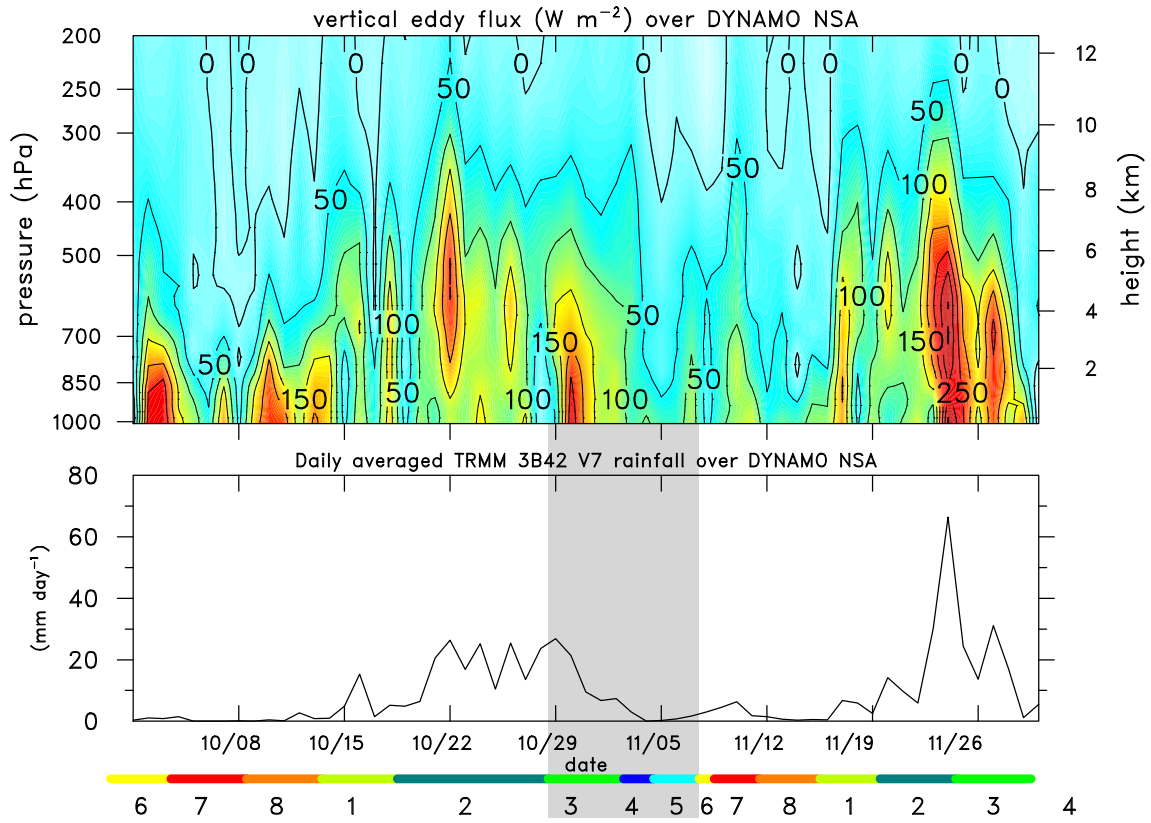


FIG. 14. Time series of daily-average values of (upper) vertical eddy moist static energy flux F ($W m^{-2}$) and (lower) TRMM 3B42v7 rainfall rate ($mm day^{-1}$) for NSA for DYNAMO SOP. Shaded region denotes period when R/V *Reville* was off station. Wheeler and Hendon (2004) RMM Index shown on lower axis.

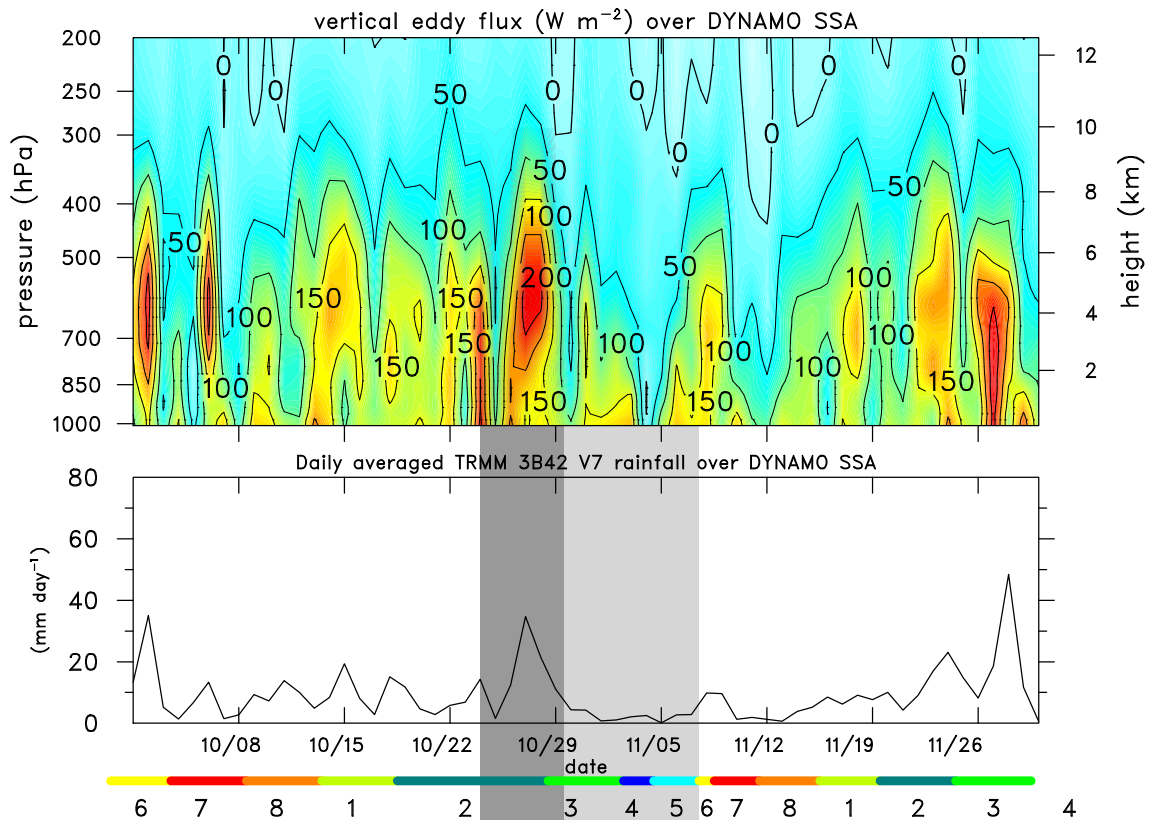


FIG. 15. As in Fig. 14, except for SSA. Dark and light vertical shaded bars indicate times when R/V *Mirai* and *Revelle*, respectively, were off station.

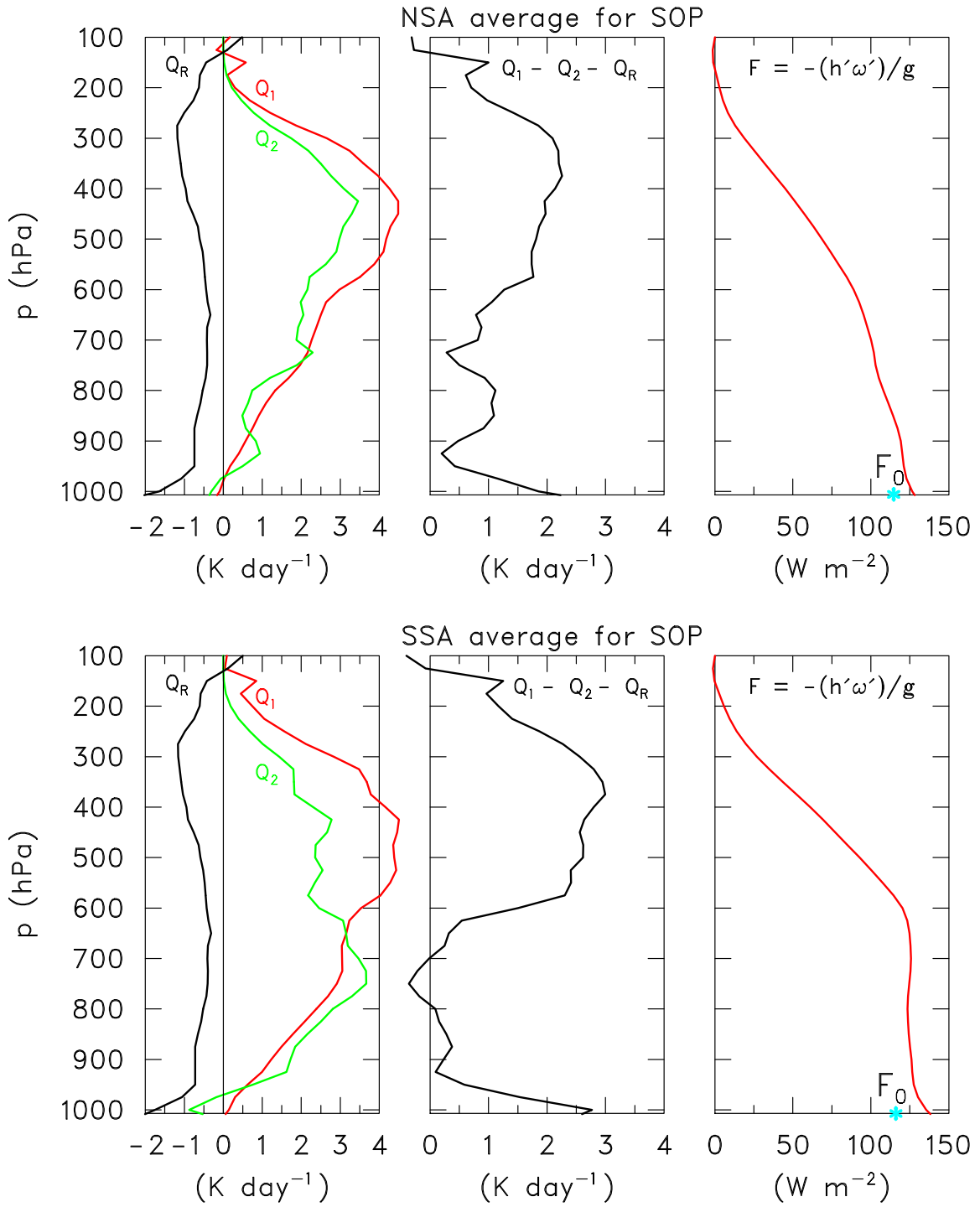


FIG. 16. SOP-mean profiles of Q_1 , Q_2 , Q_R , $Q_1 - Q_2 - Q_R$, and F (K day⁻¹) for (upper) NSA and (lower) SSA. Surface sensible plus latent heat flux (F_0) from TropFlux is indicated by asterisks on bottom axes.